Dalton Transactions

Accepted Manuscript

ROYAL SOCIETY OF CHEMISTRY

www.rsc.org/dalton

Phase Transitions and Interface Phenomena at Cryogenic Temperature Domain of a Niobate Nanostructured Ceramic

S. Lanfredi[1], C. Darie[2], F. S. Bellucci[3], C. V. Colin[2], M. A. L. Nobre[1]*

[1] Fac de Ciências e Tecnologia – FCT, Univ Estadual Paulista – UNESP, P.O Box 467, Presidente Prudente-SP, 19060-900, Brazil.

[2] Institut Néel, CNRS et Université Joseph Fourier, B.P. 166, F-38042 Grenoble Cédex 9, France.

[3] Brazilian Ministry of Science, Technology and Innovation – MCTI, Brasília – DF, 70067-900, Brazil.

Abstract

Powder neutron diffraction and dielectric spectroscopy were used to investigate both crystallographic and dielectric permittivity properties of a $Sr_2KNb_5O_{15}$ single phase ferroelectric oxide with nanosized grains ranging from 35 nm to 90 nm. Measurements were carried out in the temperature range from 10 K (cryogenic) up to 550 K. All neutron diffraction data were indexed on the basis of a tetragonal double unit cell. From 10 K to room temperature the space group of the $Sr_2KNb_5O_{15}$ ferroelectric phase was considered the *P4bm*. The refinement of the paraelectric phase (at 550 K) was determined in the centrosymmetric space group *P4/mbm*. Dielectric spectroscopy measurements were performed in a thermal cycle. A set of four phase transitions non related to symmetry changing was detected from Rietveld analysis of neutron powder diffraction data. During a thermal cycle, at cryogenic temperature domain, strong thermal hysteresis is developed. Both phase transition and thermal hysteresis were correlated. These phenomena are associated to Nb-cation atomics displacement in the NbO_6 octahedral along *c-axis* direction and of domain with different frequencies involving grain as well as an excess of interfaces ascribed to the grain boundary. The bulk/grain boundary interfaces in nanostructured ceramics are correlated with the thermal stability phenomenon.

*Author to whom correspondence should be addressed: e-mail: nobremal@fct.unesp.br
Phone: +55 18 3229-5746; FAX: +55 18 3221-5682

Introduction

Ferroelectric niobates exhibiting tetragonal tungsten bronze TTB-type structure have gained interest due to the set of distinct crystalline sites and high anisotropy of their crystalline structure. The TTB-niobate structure can be further described by the minimal chemical formula $(A1)(A2)_2C_2Nb_5O_{15}$, where *A1*, *A2*, and *C* denote different sites in the crystal structure. *A1* and *A2* occupy 12-fold coordinated and 15-fold coordinated tunnels, respectively. C sites are typically vacant [1]. The Nb cations occupy two non-equivalent octahedral sites called *2b* and *8d* sites. The TTB-type structure enables the substitution of a wide-variety of cations on the *A1*, *A2* sites, in particular alkali and alkaline earth. Other substitutions based on the transition metal are viable on the niobium site [2]. The size and type of replacement of ions in different sites of the structure have a significant effect on the dielectric properties [2]. In a general way, octahedral distortions resulting of a specific cation occupation have been observed. The octahedral distortion can modulate and/or stabilize properties such as: ferroelectricity, piezoelectricity and second-harmonic generation [3].

In TTB compounds as $Sr_{1-x}Ba_xNb_2O_6$, $Pb_xBa_{1-x}Nb_2O_6$ and $(K_xNa_{1-x})_{0.4}(Sr_yBa_{1-y})_{0.8}Nb_2O_6$ the existence of phase transition, at cryogenic temperature domain, has been related to transition from tetragonal (4*mm*) to monoclinic (*m*) space group [4]. However, the question about the TTB-type structure stability seems open. There is a tendency to correlate the occupation of different cations on the pentagonal and tetragonal sites by alkaline and alkaline earth with a thermal stability of the crystalline structure, transitions from one symmetry to another symmetry. Cryogenic temperature anomalies have also been reported by dielectric and pyroelectric measurements [5], cooperative rotations of the oxygen cage can be one of the possible origins of this phenomenon. Another hypothesis is a re-entrant phenomenon, which has been related to a decreasing of the long-range interaction of structural dipole on cooling [6]. This phenomenon has been reported in perovskite-type materials even though it is still not completely understood.

At low temperature the dielectric behavior has been assigned to the inherent randomness of the structure generated by vacancies or cationic disorder, both giving rise to the vanishing of the macroscopic polarization [5]. Single crystal displays anisotropic physical properties with respect to crystal axis, however, in general, conventional polycrystalline ceramic is usually composed of randomly oriented grains (1-100 μm), thus yielding an average of its anisotropic properties. In all case, the electric and dielectric phenomena are dominated by the bulk response.

Among the TTB-structure oxides, strontium potassium niobate oxide, $Sr_2KNb_5O_{15}$, has attracted particular interest. $Sr_2KNb_5O_{15}$ is non-centrosymmetric material that due the multiplicity of unitary cell and high crystallinity structure leads to an unipolar ferroelectric lead free TTB material[7] that belongs to the class of ceramic compounds that exhibit texturing by application of pressure or magnetization[8,9], piezoelectric, catalytic and dielectric properties [10,2]. Despite of some studies on the electrical properties of $Sr_2KNb_5O_{15}$, none of them have been dedicated to the clarifying of dielectric properties of ceramics with nanosized grains, at the cryogenic temperature. For ferroelectric oxides, the maximum of the permittivity and its broad character have been assigned to the particular conditions of polarization phenomenon steaming phase transitions termed ferroelectric-paraelectric [11]. However, none study has been addressed on the structural stability and interface influence on electrical properties of the $Sr_2KNb_5O_{15}$ nanostructured ceramic. In this sense, the mechanism of grain growth and densification during the sintering phenomenon involving structure with low symmetry and multiplicity of cell has shown crystals with high aspect ratios. However, the mechanism responsible for the high aspect ratio of the grain has been little investigated. In this case, the sintering of the ceramic occurs in the solid state. This sintering process involves breakage and rearrangement of grains, forming grains of smaller aspect ratio. This process can be modulated by the specific characteristics of the interface as strain and stress level.

This work provides a comprehensive report on the structural thermal stability of the $Sr_2KNb_5O_{15}$ powder investigated by neutron diffraction and the dielectric-permittivity properties at cryogenic temperatures of $Sr_2KNb_5O_{15}$ ceramic with microstructure based on nanosized grains.

The correlations between thermal hysteresis of dielectric permittivity and non structural phase transitions are established. As a function of nanostructured microstructure, the excess of grain boundary parameters are stressed three times of interfaces addressed on nanograin geometry, taking into account nanosize grains based on the excess of grain boundary determining majority response. Each one of the type of interfaces exhibits a relaxation frequency characteristic, all of them below of 1 KHz, one of them operates in domain of the infrasound.

Experimental

Synthesis Procedure

$Sr_2KNb_5O_{15}$ single phase nanostructured powder was synthesized by the Modified Polyol method[7]. As a whole, this method gives rise a better control of cations homogeneously distributed in the precursor, a low calcination temperature, a single phase and high specific surface area powder. The starting reagents for the powder synthesis via chemical route were nitric acid HNO_3 (99.5% Reagen), strontium carbonate $SrCO_3$ (99.0% Reagen), potassium carbonate K_2CO_3 (99.0% Reagen), ethylene glycol $HOCH_2CH_2OH$ (98.0 % Synth) and niobium ammonium oxalate $NH_4H_2[NbO(C_2O_4)_3].3H_2O$ (CBMM-Brazil). All salts were dissolved in nitric acid under continuous stirring in a beaker. In the sequence, 100 ml of ethylene glycol was added. The solution temperature was heated at 90 ^oC, leading to the decomposition of nitrate group, a phenomenon similar to the process developed in the Pechini method [12]. After this process, a gel polymeric is obtained. Then, the gel polymeric is maintained in the beaker undergoes a primary calcinations in a furnace type box. The heating cycle was carried out using two steps from room temperature. In the first step, the temperature was increased using a heating rate equal to 10 ºC/min up to 150 ºC. At this point, the temperature was kept constant during 30 min. In the second step, the temperature was increased at 300 ºC, being maintained during 1 hour. After the cycle, the furnace was cooling to the natural rate. The nitrogen flux was constant at 500 mL/min during the heating and the cooling cycle.

This process leads to the partial gel polymeric decomposition forming an ash with moderate expansion level, which consists in a brittle reticulated material. This material was deagglomerate (350 mesh) in an agate mortar being termed precursor. The precursor was calcinated in a tube furnace in oxygen atmosphere with flux of 300 mL/min. The time and temperature parameters, of the precursor powder, were optimized to obtain $Sr_2KNb_5O_{15}$ single phase powders with high crystallinity. The calcination was carried out at 1150 ºC during 10 hours, using heating rate equal to 5 ºC/min.

Neutron Diffraction Measurements

Neutron powder diffraction (NPD) data were collected on the CRG-D1B instrument of the Institut Laue Langevin – Grenoble. A 1.28 Å wavelength from the (311) reflection of a Ge monochromator was used. The sample was put inside a cylindrical vanadium placed in an orange cryostat. Long time measurements were carried out at selected temperatures (10, 300 and 550K). The sample was cooled down to 10 K then slowly heated up to 550 K while powder neutron diffraction data were recorded ‘‘on the fly’’ about every 5 minutes. The neutron powder diffraction data were analyzed by the Rietveld method using the Fullprof Software [13]. Powder data and experimental conditions are listed in Table 1. The crystallite sizes (D) and microstrain (ε) were calculated using the Williamson-Hall equation [14]:

$$\beta \frac{cos(\theta)}{\lambda} = \frac{1}{D} + 4\varepsilon \frac{sin(\theta)}{\lambda} \qquad (1)$$

where θ is the diffraction angle, λ is the wavelength of incident radiation and β is the broadening of the diffraction line measured at half of the maximum intensity. The characteristic plot Williamson-Hall corresponds to the graph of $\beta\cos(\theta)/\lambda$ *versus* $4\sin(\theta)/\lambda$. Here, $4\sin(\theta)/\lambda$ is on the x-axis. Each point is assigned to a diffraction line.

After point collection, a linear regression should give a linear fit. The crystalline size was derived from the y-intercept of the fit. The lattice strain η was extracted from the slope of the fit curve [3]. Parameters average crystallite size (D) and lattice strain (η) of the $Sr_2KNb_5O_{15}$ nanostructured powder along (*00l*) plane as a function of temperature were listed in Table 2. Both parameters were derived in accordance with Eq. (1). A small crystallite size was achieved with an increase in the microstrain lattice at 10 K. A major increase of the average crystallite size, D = 22 nm, was observed with a decrease of the microstrain value at room temperature. At high temperture (550 K), the microstrain value undergoes an increasing five times reaching values of the order of 10^{-4}. In a general way, microstrain has been visualized as due a local fluctuations of the interplanar spacing, hence its occurrence induces the anisotropic physica properties. Here, the lattice anisotropy and static disorder steams from specific occupation of the pentagonal site or A2-site in a *quasi*-statistical occupation.

Microstructure Analysis

Prior to the sintering, the powder was uniaxially pressed into pellet form of 8x2 mm dimension. The green compact was sintered at 1553 K in air for 2 h at a heating rate of 2.0 K/min. Relative density equal to 97 % of the theoretical density was reached. Microstructure was characterized using scanning electron microscopy – SEM (Zeiss DSM 962).

Electrical Measurements

Electric measurements were carried out by impedance spectroscopy over a complete thermal cycle. Electrodes were deposited on both faces of the sample with a platinum paste coating (TR-7905 –Tanaka). After complete solvent evaporation, the electrode/ceramic was dried at 1073 K for 30 min. Measurements were taken in the frequency range of 5 Hz to 13 MHz, with an applied potential of 500 mV using an Impedance Analyzer Alpha N High Resolution Dielectric from Novocontrol GmbH, which was controlled by a personal computer.

The sample was placed in a sample holder with a two-electrode configuration. Measurements were taken from room temperature to 800 K in 50-K steps at a heating rate equal to 1.0 K/min in air. A 30-min interval was used prior to thermal stabilization before each measurement. The data were plotted using the complex plane formalism ortho-normalized, *Z'(ω) versus Z''(ω)* plot, and analyzed with Boukamp's EQUIVCRT software.

Dielectric spectroscopy characterization was performed in the frequency range of 1 kHz to 1 MHz and a temperature range of 15K to 800 K.

The complex permittivity function $\varepsilon^{*}(\omega)$ was derived from the impedance function, $Z^{*}(\omega)$:

$$Z^{*}(\omega) = \sum_{i}^{n} Z_i^{*}(\omega) = Z_1^{*}(\omega) + Z_2^{*}(\omega) + \ldots + Z_n^{*}(\omega) \qquad (2)$$

$$Z^{*}(\omega) = \sum_{i}^{n} Z_i^{'}(\omega) + j\sum_{i}^{n} Z_i^{''}(\omega) = \sum_{i}^{n} Re_i(Z) + j\sum_{i}^{n} Im_i(Z) \qquad (3)$$

where $Z^{*}(\omega)$ is an apparent response composed by the contribution of all electroactive components of the system and can be represented by Eq. (2) and (3), n is the number of electroactive component of the system. The most frequent response to $Z^{*}(\omega)$ is a semicircle which can be decentralized or not be. In a general way, this semicircle is an apparent response which represents a combination of two or more semicircles, as example grain and grain boundary [2]. Here there is a general role to understand this apparent response. Each semicircle can be fulfil observed on the impedance diagram only if the relaxation frequency that ascribes each semicircle differ at least of two orders of magnitude.

The impedance can be represented by the following equation:

$$Z^{*}(\omega) = R_{\infty} + \frac{(R_0 - R_{\infty})}{1 + (j\omega RC)^{1-\theta}} = \begin{cases} Z'(\omega) = R_{\infty} + \dfrac{(R_0 - R_{\infty})\left[1 + (\omega RC)^{1-\theta}\,\mathrm{sen}\,\frac{1}{2}\theta\pi\right]}{1 + 2(\omega RC)^{1-\theta}\,\mathrm{sen}\,\frac{1}{2}(\theta\pi) + (\omega RC)^{2(1-\theta)}} \\ Z''(\omega) = -\dfrac{(R_0 - R_{\infty})(\omega RC)^{1-\theta}\cos\frac{1}{2}\theta\pi}{1 + 2(\omega RC)^{1-\theta}\,\mathrm{sen}\,\frac{1}{2}(\theta\pi) + (\omega RC)^{2(1-\theta)}} \end{cases} \qquad (4)$$

where R_∞ and R_0 represent the resistance at high and low frequency, respectively, and θ represents the decentralization angle, following the Cole-Cole theory [15]. θ can be derived from the following equation:

$$n = \frac{2\theta}{\pi} \quad (5)$$

Typically, for polycrystalline ceramic systems, the impedance can be described by two electroactives contributions assigned to the grain (G) and the grain boundaries (GB). From Eq. (2) determines the impedance of the system given by Eq. (6):

$$Z^*_{CERAMIC}(\omega) = Z^*_G(\omega) + Z^*_{GB}(\omega) \quad (6)$$

From of the function transformation $\varepsilon^*_{CERAMIC}(\omega) = [j\omega\varepsilon_0 \Lambda Z^*(\omega)]^{-1}$, these components of transformation relationships are given by the Eq. (7), as follows [16]:

$$\varepsilon^*_{CERAMIC}(\omega) = \frac{1}{j\omega\varepsilon_0 \Lambda Z^*(\omega)} = \begin{cases} \varepsilon'(\omega) = -\frac{1}{\Lambda\omega\varepsilon_0}\left(\frac{Z''(\omega)}{|Z^*|^2}\right) \\ \varepsilon''(\omega) = \frac{1}{\Lambda\omega\varepsilon_0}\left(\frac{Z'(\omega)}{|Z^*|^2}\right) \end{cases} \quad (7)$$

where Λ represents the geometric factor of the cell, ω represents the angular frequency ($\omega = 2\pi f$), ε_0 represents the vacuum permittivity constant (8.8542×10^{-12} F/m), and $|Z^*(\omega)|$ represents the module of the impedance; $\varepsilon'(\omega)$ and $\varepsilon''(\omega)$ represent both the real and imaginary component of the complex dielectric permittivity $\varepsilon^*(\omega)$, respectively.

Results and discussion

Structural Analysis by Neutron diffraction

The thermal evolution of the crystalline structure of $Sr_2KNb_5O_{15}$ nanostructured powders from neutron diffraction in the temperature range from 10 to 550 K and on the scattering for two 2θ intervals corresponding to $2\theta = 0.8^o – 128.00^o$ is shown in Fig. 1. All neutron diffraction data were indexed on the basis of a tetragonal unit cell. At 10 K, the refinement for the $Sr_2KNb_5O_{15}$, i.e. ferroelectric phase, was carried considering as a starting model the *P4bm* space group (non-centrosymmetric group). The structural model used for the refinement was the same as for the one described at high temperature phase as follows: (i) trigonal site vacant, (ii) pentagonal site occupied by K^+ and Sr^{2+} ions refined with independent positions (8d Wyckoff Position), (iii) anisotropic thermal factor for O3 and O5.

The Rietveld plot for $Sr_2KNb_5O_{15}$ with the experimental, calculated and difference neutron diffraction profile at 10 K is shown in Fig. 2. Both atomic parameters and atomic displacement parameters derived by the refinement are listed in Table 3(a). Table 3(b) shows the thermal factor of O3 and O5 refined with an anisotropic model. Bonds distances for $Sr_2KNb_5O_{15}$ at 10 K are listed in Table 3(c). To the difference to the high temperature centrosymmetric space group *P4/mbm*, the non-centrosymmetric space group *P4bm* allows polar displacements along the c-axis, and all the z-coordinates of the atoms are refinable.

At 550K, the refinement procedure of the $Sr_2KNb_5O_{15}$, *i.e.* paraelectric phase [17], was done using as input data the structure determined in the centrosymmetric space group *P4/mbm* (No. 127). Each pentagonal site (4*c* (x, x+1/2, z)) was assumed as being statistically occupied by K^+ and Sr^{2+} cations and each tetragonal site (2a (0,0,z)) occupied by a Sr^{2+} cation. The trigonal site was considered vacant. Cations Nb^{5+} occupy two non-equivalent octahedral sites called *2b* and *8d* sites. The refinement gives a good set of physical parameters except for the temperature factor of the pentagonal 4c site occupied by K^+ and Sr^{2+} cations that was found to be particularly great.

This find is a strong evidence for some kind of disorder event within the pentagonal site. Since, both K^+ and Sr^{2+} cations do not exhibit a same valence, their positions should be distinct to respect bound valence sum rules. Then, further setup to refinement should taking in account K^+ and Sr^{2+} cations in two different 8d Wyckoff position. Therefore, a proper refining of positions of two atoms were independently carried out. Whereas the Sr^{2+} cation keeps almost the 4c position in the half of the pentagonal site, the K^+ cation adopts two equivalent positions getting close to the oxygen O3, see Fig. 3. The thermal factor of O3 and O5 were refined with an anisotropic model, see Table 4(b). Indeed these two oxygen surround the pentagonal site in the (a,b) plane and are case sensitive to a "kind of intrinsic site disorder" property called static disorder. The Rietveld plot for $Sr_2KNb_5O_{15}$ with the experimental, calculated and difference neutron diffraction profile at 550K are shown in Fig. 2. Structural parameters are listed in Table 4(a). Fig. 3 shows the graphic representation of the unit cell obtained for $Sr_2KNb_5O_{15}$ powder at 550K. *A priori*, niobium atoms are coordinated to six oxygen atoms, four of them are located on the same plane as the niobium atoms. Other two oxygen atoms are above and below of the plane, respectively. This condition is favourable for the formation of an M site octahedral in the structure [3]. In $Sr_2KNb_5O_{15}$ structure, Nb^{5+} cations can be differentiated as Nb(1) and Nb(2), because they occupy two non-equivalent octahedra, as shown in Table 4(a). Both types of niobium atoms form their own chains based on the vertex-shared octahedra [NbO_6]. Bonds distances between atoms of $Sr_2KNb_5O_{15}$ are listed in Table 4(c).

[NbO_6] Distortion Mode Analysis

A distorted structure can be described as a parent crystalline structure plus a static symmetry-breaking structural distortion. A set of crystalline structures is considered pseudosymmetric with respect to some configuration of higher symmetry. A group-subgroup relation exists between the space groups of the parent and the observed structures.

The distortion relating both phases can be decomposed into contributions from different modes with symmetries given by the irreducible representations (IRs) of the parent space group. This idea is the starting point of the well-known Landau's theory, based on the identification of the order parameter, *i.e.*, the mode(s) driving the stabilization of the distorted phase. In a general way, a structure description in terms of symmetry modes separates the correlated atomic displacements, which are fundamental for the phase stability from those which are marginal. It introduces a physical hierarchy among the structural parameters, that can be valuable for investigating the physical mechanisms which stabilize these phases. Since, structural distortions in $Sr_2KNb_5O_{15}$ may be related to the ferroelectric polarization, this procedure is further adequate to reveal specific links between structure and ferroelectric properties in this quite complex system.

Symmetry-mode analysis was carried out on ferroelectric phase using AMPLIMODES program [18]. The mode decomposition of the $Sr_2KNb_5O_{15}$ experimental P4bm ferroelectric structure with respect to its experimental P4/mbm parent structure (paraelectric) is summarized in Table 5. Two different IRs are possible by symmetry: GM1+ and GM3-. The global distortion amplitude is 0.7479Å. GM1+ is a distortion mode that allows the atomic displacement of the atoms in the (a,b) plane, whereas the GM3- distortion mode allows the displacement of the atoms along the c-direction. Based on the relative amplitude of the IRs, one can see that distortion amplitude of GM1+ is zero and that GM3- is responsible for all the distortion. This behaviour means that the paraelectric-ferroelectric transition does not affect the atomic position within the basal plane but only along the c-axis which is the polar direction. A standard scheme of the GM3- distortion mode is shown in Fig. 4. Whereas apical oxygen (O3 and O5) do not show significant displacement, basal oxygen and niobium atoms move along the c-axis in opposite direction. The relative displacement of Nb and oxygen ions give rise to the off-centering of the Nb ion within its octahedral cage.

At 10 K, from comparison between the Nb-O average distances, both Nb(1)-O_6 and Nb(2)-O_6 octahedral show a significant relative off-center displacement of Nb ion along *c*-axis.

This phenomenon leads to unequal Nb(1)-O(5) bond lengths of 1.85(4) and 2.06(5)Å and unequal Nb(2)-O(3) bond lengths of 1.90 (4) and 2.02 (4) Å, see Table 3(c). The inspection of the two [NbO_6] octahedra neighborhood shows that the relative displacement of the ions in the Nb(1) site is larger than the Nb(2) site. These results would suggest that Nb(1) site dominates the polar response in these materials. In this way, the crystalline structure is maintained while the space group changes as function of polyhedral distortions.

Phase Transition

The evolution of the unit cell volume and lattice parameters as function of temperature is shown in the Fig. 5 and 6, respectively. Lattice parameters *a*, *b*, *c* and unit cell volume *V* were derived on a wide range of temperatures, from 15 up to 550 K, taking into account tetragonal symmetry. Both Fig. 5 and 6 show distinct magnitude of values between *a=b* and *c* and its correlation with increasing as function of temperature. The lattice anisotropy characteristic ensures a singular difference of magnitude of expansion of the lattice parameters.

Sequential Rietveld refinement was performed considering at low temperature the space group *P4bm* and at high temperature the space group *P4/mbm*. Space group changing occurs at the temperature of the transition ferroelectric-paraelectric, a non structural transition, which was determined be 408(5)K. From this temperature, the R factor increase when doing the sequential refinement: from low to high temperature using *P4bm* space group and from high to low temperature using *P4/mbm* space group. This temperature corresponds to the Curie's Temperature determined at 408 K by the permittivity measurement, see Fig. 14 discussion. Therefore, this result assigned to the ferroelectric-paraelectric transition. Here, can be stressed that the ferroelectric-paraelectric transition is accompanied by changing in the c-axis parameter which is the polar direction, see Fig. 6.

At high temperature domain, the static disorder tends to static order, since magnitude of niobium-off-center reach to zero, space group should reach to center-symmetric space group.

The c-axis dilatation when decreasing the temperature can be considered as an indirect signature of the NbO_6 octahedron distortion and therefore of the development of the ferroelectric polarization. According to Fig 6, lattice parameters *a* and *b* with *a=b* decreases in a regular way as function of temperature decreases. Also, the Curie's temperature stays invariant. As a whole, an anomaly in the lattice parameters can be observed around 255 K, anomaly more visible in the evolution of the unit cell volume (Fig. 5). These bumps can be related to the anomalies observed in the permittivity curve (Fig. 14). In Fig. 5 intense lattice shrinkage can be observed in the temperature range investigated and two regions are remarkable. The first is linear in essence at T> 408 K and second one non-linear at T< 408K.

The idea of anisotropy is correlated to the departure of an ideal structure or cubic structure. *A priori*, the parameter anisotropy crystalline describes very well distortions in cubic unitary cell, distorted cubic and tetragonal, as an example, classic structures as $BaTiO_3$ and $SrTiO_3$ can be mentioned. The ratio between the lattice parameter *a* and *a* distorted, or *a* and *b* provided a value that characterize magnitude of anisotropy of the crystalline structure. Taking account previously both mentioned structures, this value stays close to 0.9. For TTB-type structures a high anisotropy factor can be defined, the term high makes a particular sense, since the unitary cell contents a tens of atoms, as a matter of fact the unitary cell is only stabilized with multiplicity of unity. Then, the parameter high anisotropy factor can be understood, as an example the high factor of anisotropy derived for the $Sr_2KNb_5O_{15}$ structure *c/a* is equal to 0.3159. At moment, there is not a correlation between structural phase transitions (symmetry changing) and high anisotropies of TTB phase transitions. Nevertheless, there is small evidence of influence of specific site occupation by cations belong to the alkaline and alkaline earth group [3], in specific the tetragonal and pentagonal sites (A1 and A2, respectively).

Here, some careful analysis should be reached with relations to terms order and disorder, in particular the term disorder should be further applied when ascribed to the fluctuations of composition. On the other hand, the specific occupation of cations in tetragonal and pentagonal sites

of the TTB-type structure can be directly related to the structural stability. Here, the tetragonal site is only occupied by Sr^{2+} cations while the pentagonal site is occupied almost in the half of 4c position by Sr^{2+} cation and with K^{+} cation occupying two equivalent positions getting close to the oxygen O3, as discussed previously. These occupations give further thermal stability to the structure. On the other hand, when the Sr^{2+} and K^{+} cations occupy the same 4c position on the pentagonal sites the structure is not stable. Thus, there is a specific occupation of the sites in TTB structure that confers its stability which is not correlated to a conventional disorder phenomenon. It is worth noting that static disorder term should be preferred.

Microstructure and Nanostructure

At room temperature, the crystalline structure of $Sr_2KNb_5O_{15}$ exhibits the space group P4bm compatible with tetragonal symmetry and Schönflies point group C^2_{4v} [19]. This point group belongs to the crystal class of type ditetragonal pyramidal with Hermann-Mauguin point group 4mm and mineral form of the fresnoite of space group P4bm, lattice parameters equal to $a = b = 8.5291$ Å, c = 5.2110 Å, V = 379.1 $Å^3$, density equal to 4.44 g/cm^3 and presents a distinct cleavage at {001} [20]. This crystal structure is of particular interest due the coincident Z parameter value equal to 2, the same value of the $Sr_2KNb_5O_{15}$ (see Table 1). Despite the $Sr_2KNb_5O_{15}$ structure to exhibit same Z value, the fresnoite shows a non large anisotropy factor $c/a = 0.6109$, while $Sr_2KNb_5O_{15}$ exhibits a great anisotropy factor of order of $c/a = 0.3159$, at room temperature. The crystal shape of fresnoite is shown in Fig. 7 [20].

Fig. 8 shows the scanning electron microscopy (SEM) image of the $Sr_2KNb_5O_{15}$ ceramic sintered at 1553 K for 2 h. The microstructure shows grain pullout, few pores and nanosized grains.

The inset shows an expanded region of Fig. 8 that exhibits some grains with anisotropic growth because the growth rate in the *c-axis* direction [001] is faster than that in the *a-axis* direction, resulting in high aspect ratio reaching to acicular (or anisotropic) growth and displacement of grains, as can be seen in G1, G2 and G3. In fact, this crystal shape is similar to the

Fresnoite shape, which can be observed in several grains of the microstructure of Fig. 8 (see inset). The Fresnoite crystal belongs to the tetragonal – ditetragonal pyramidal class (4mm). In this symmetry element there is a single four fold axis and four mirror planes with all three angles = 90 ^{o}. Two axes, *a* and *a′* are equal to each other, but they are either shorter or longer than the **c** axis. Crystals of this group are hemimorphic, *ist est* different top and bottom (see Fig. 7). This feature is identified at almost all grains of the microstructure. In this sense, due to the high anisotropy associated to the crystalline symmetry of each grain, not all sides of the grain boundary have the same surface energy. However, there is a high frequency of grain boundary between three grain exhibiting angles of 120^{o}, but is possible to find angles of 90^{o}. However, if the solid-state sintering is considered, the grain size increases and some grains must shrink or disappear [21]. The driving force for the process is the difference in energy between the fine grained material and the larger grain size resulting from the decrease in grain boundary area and the total boundary energy. A more detailed study from analysis of an expanded region (inset of Fig. 8) is shown in Fig. 9. According to Fig. 9, grains are formed by a substructure of ≈ 20 nm. The formation of theses substructures are due the displacement of grains that can be observed along of grains of size of 0.3 μm, 0.55 μm and 0.63μm of length and of 0.20 μm and 0.25 μm of wide. Such substructure seems be generated by perpendicular forces to c-axes, which leads to the cleavage phenomenon. Here, the cleavage phenomenon can be reached with a multi diversity of microstructure component. In specific, microstructure phenomenon emerges from the set of concepts. Ceramics exhibiting high texturization can be engineered from non cubic symmetry, adequate *c/a*, multiplicity of unity cell and cleavage phenomenon being operational.

Impedance Spectroscopy Analysis

Fig. 10 shows the $Sr_2KNb_5O_{15}$ ceramic impedance diagram, normalized by the geometric factor, and theoretical adjustment attained at 600 K. According to Fig. 10, points on the plot represent the experimental data, while the continuous line represents the theoretical adjustment.

The agreement between the experimental points and the theoretical curve is excellent. The theoretical adjustment follows the Cole-Cole theory [15]. The deconvolution of the electrical response is an alternative approach to derive all electric and dielectric contributions [22]. The bulk and grain boundaries properties can be unequivocally derived via Boukamp's formalism [23]. In this formalism, the non-ideal character of the polarization phenomenon is represented by a *Q* parameter instead of a *C* parameter. *Q* has been interpreted as a non-ideal capacitance that is physically determined by the parameter Y_o and the exponent *n* with $n \leq 1$, see Eq. (10). Y_o tends to approach an ideal capacitance (*C*) when the exponent *n* tends toward a value of 1.

By hypothesis, the non-ideal character of *Q* is only assigned to a distribution of the relaxation times, which is the origin of the semicircle decentralization observed in Fig. 10. Thus, the parameter $Q(Y_o,n)$ should have an equivalent parameter in the form of an ideal capacitance C before it is an adequate interpretation of the electric properties. In Boukamp's formalism, the impedance of a circuit $[RQ(Y_o,n)]$ series is given by:

$$Z^*(\omega) = \frac{R}{1 + RY_o(j\omega)^n} \tag{9}$$

The parameters *R*, Y_o and *n* are extracted by theoretical fitting. *C* is derived from:

$$C = R^{(1-n/n)} Y_o^{(1/n)} \tag{10}$$

In this work, the exponent *n* is close to unity (quasi-Debye), depending on the measurement temperature. The electric response is well represented by four equivalent parallel *RC* circuits in series, where *R* represents the resistance and *C* represents the capacitance.

An equivalent electric circuit and its respective resistance and capacitance components were derived for $Sr_2KNb_5O_{15}$ ceramic, as shown in the Fig. 11. At low frequency (< 10^3 Hz), contributions represent the grain boundary contributions to the electric response. At high frequency (>10^3 Hz), contributions corresponds to the specific properties of the grain or bulk. The several contributions of the grain boundary can be explained by different arrangements of the grains in the

microstructure, as shown in the inset of Fig.10. Due to the high anisotropy associated to the crystalline symmetry, the grain boundaries not have the same energy and crystal surface in all sides. In this sense, there is grain boundary forming angles of 90^{o} (grain boundary II) and a high frequency of grain boundary between three grain exhibiting angles of 120^{o} (grain boundary III), a classical arrangement signalizing a sintering stage close to the final (100% of theoretical density), as shown in the inset of Fig. 10.

Values of resistance, capacitance and relaxation frequency parameters were derived for the grain and grain boundary of the $Sr_2KNb_5O_{15}$ nanosized ceramic. Values are represented in the electric circuit of Fig. 11, which are listed in Table 6. The grain boundary interfaces characterized via electric circuit equivalent methods show the following relaxation frequency ordering: f_{GB}^{I} (interface type I) > f_{GB}^{II} (interface type II) > f_{GB}^{III} (interface type III). Taking in account Table 6, if $n \rightarrow 1.0$, the dielectric behavior is ideal. In other words, there is a single relaxation frequency. On the other hand, if $n \rightarrow 0.5$ the dielectric response deviates from an ideal response. In this case, the single relaxation frequency turns the most frequent relaxation frequency. According to Figure 10 and Table 6, the grain boundary I (type I interface) is equivalent to the contact planes of the prism formed, as shown in Fig. 7. Within all interfaces displayed, the interface Type III is the most irregular, with a larger number of defects and cleavage phenomenon, as schematized in Fig. 12. In nanoceramic, as a function of scattering of phonon, only mechanical phonons characteristic at crystalline lattice seems be operational. Furthermore, all relaxation frequencies belong to range termed audio-frequency, the set of frequencies detected by human and mammal hearing.

As an example, the relaxation frequency of grain boundary of type II (f_{GB}^{II} = 280 Hz being the relaxation time $\tau_{GB} = 3.57x10^{-3}$s) is equivalent to the average frequency of voice sensor, as and as of a mechanical filter, resonator as well as of the prosthesis of inner voice of a little girl. Also, frequency equal 11 Hz is too low for be generated or detected by a human being, but an elephant can be easily to hear this sound. This range of frequency is able of contours obstacles of great

dimensions, reaching kilometers of distance. In this sense, this nano-ceramic investigated can be used as a filter or a sensor in ultra-low frequency domain.

Fig. 13 shows both real and imaginary components of the impedance diagram for the $Sr_2KNb_5O_{15}$ ceramic measured at 600 K, with superposition of the adjustment curve generated from the Eq. (11). The best adjust was derived with i= 4, in according to Eq. (3), see Fig. 10 discussion. Points on the plot represent the experimental data and the continuous line represents the theoretical adjustment carried out via Eq. (11). As highlighted previously, excellent agreement between the experimental and theoretical curves was obtained, validating the physical parameters derived for the grain and grain boundary.

Eq. (11) relates the contribution of the grain (G) and grain boundaries (GB1, GB2 and GB3) from Eq. (4).

$$Z^{*}_{NANOCERAM}(\omega)=\left[\begin{array}{l} R_{\infty}+\dfrac{(R_G-R_{\infty})}{1+(j\omega R_G C_G)^{n_G}}+\dfrac{(R_{GB1}-R_G)}{1+(j\omega R_{GB1}C_{GB1})^{n_{GB1}}}+ \\ \quad +\dfrac{(R_{GB2}-R_{GB1})}{1+(j\omega R_{GB2}C_{GB2})^{n_{GB2}}}+\dfrac{(R_{GB3}-R_{GB2})}{1+(j\omega R_{GB3}C_{GB3})^{n_{GB3}}} \end{array}\right] \quad (11)$$

Likewise, the Eq. (11) can be expressed in terms of its real $Z'_{NANOCERAM}(\omega)$ and imaginary $Z''_{NANOCERAM}(\omega)$ components, as shown below:

$$Z'_{NANOCERAM}(\omega)=\left[\begin{array}{l} R_{\infty}+\dfrac{R_G-R_{\infty}}{1+(\omega R_G C_G)^2}+\dfrac{R_{GB1}-R_G}{1+(\omega R_{GB1}C_{GB1})^2}+ \\ +\dfrac{R_{GB2}-R_{GB1}}{1+(\omega R_{GB2}C_{GB2})^2}+\dfrac{R_{GB3}-R_{GB2}}{1+(\omega R_{GB3}C_{GB3})^2} \end{array}\right] \quad (12)$$

$$Z''_{NANOCERAM}(\omega)=-\left[\begin{array}{l} \dfrac{(R_G-R_{\infty})(\omega R_G C_G)}{1+(\omega R_G C_G)^2}+\dfrac{(R_{GB1}-R_G)(\omega R_{GB1}C_{GB1})}{1+(\omega R_{GB1}C_{GB1})^2}+ \\ +\dfrac{(R_{GB2}-R_{GB1})(\omega R_{GB2}C_{GB2})}{1+(\omega R_{GB2}C_{GB2})^2}+\dfrac{(R_{GB3}-R_{GB2})(\omega R_{GB3}C_{GB3})}{1+(\omega R_{GB3}C_{GB3})^2} \end{array}\right] \quad (13)$$

Substituting values of R-C of each interface into in Eq. (11), the theoretical adjustment is reached. The equation (14) shows the parameter values derived from the theoretical adjustment at 600 K from the Eq. (11):

$$Z^{*}_{\mathrm{NANOCERAM}}(\omega)=\left[\frac{(1.81\mathrm{x}10^{5})}{1+(j\omega \mathrm{x}1.81\mathrm{x}10^{5}\,\mathrm{x}\,2.40\mathrm{x}10^{-10})^{0.98}}+\frac{(2.77\mathrm{x}10^{6}-1.81\mathrm{x}10^{5})}{1+(j\omega \mathrm{x}2.77\mathrm{x}10^{6}\,\mathrm{x}\,7.07\mathrm{x}10^{-11})^{0.99}}+\right.$$
$$\left.+\frac{(4.36\mathrm{x}10^{6}-2.77\mathrm{x}10^{6})}{1+(j\omega \mathrm{x}4.36\mathrm{x}10^{6}\,\mathrm{x}\,1.30\mathrm{x}10^{-10})^{0.99}}+\frac{(5.87\mathrm{x}10^{5}-4.36\mathrm{x}10^{6})}{1+(j\omega \mathrm{x}5.87\mathrm{x}10^{5}\,\mathrm{x}\,2.44\mathrm{x}10^{-8})^{0.89}}\right] \quad (14)$$

Summarizing, in this work has been identified, in the system investigated ($Z^{*}_{\mathrm{NANOCERAM}}(\omega)$), three grain boundary contributions (GB1, GB2 and GB3) ascribed to three distinct interfaces each one with different physical chemistry characteristics. Both grain and grain boundary contributions exhibit some decentralization angle following the Cole-Cole theory [15], see Eq. (4) and Eq. (11). The small semicircle definition in electric response is due to similar values of most frequent relaxation time, which is correlated to each relaxation phenomenon detected, semicircle assigned to the grain and another to the grain boundaries. A good visualization for semicircle on the Z'(ω) *versus* Z"(ω) can be only attained, whether in two subsequent mechanism of relaxation both values differ, at least, of three orders of magnitude. Otherwise, semicircles present some overlapping degree, based on a response very close at similar frequencies. This overlapping increase with decreasing of magnitude of the difference between most frequent relaxation time value [22].

Temperature Dependence- Dielectric Behaviour

Fig. 14 shows the real part ε'(ω) and the imaginary part ε"(ω) of the complex dielectric permittivity ε*(ω) as a function of temperature at several frequencies for a heating cycle. A visual inspection of curves shows two broad peaks or anomalies in both the ε'(ω) and ε"(ω) curves. Considering the peak-superposition phenomenon [16], an apparent peak in ε'(T) is closely centered at 255 K as a shoulder with a very broad peak, while a defined peak is positioned at 408 K. A broad dielectric maximum ε'(T) at around 240 K and a main peak at 518 K corresponding to the FE-PE

transition have been reported in $Sr_2NaNb_5O_{15}$ ceramic [3]. The broad maximum found at around 240 K has been assigned to a relaxor-like phenomenon of this material at low temperature [24]. The maximum shifts to higher values as frequency increases following the empirical Vogel-Fulcher law [25]. This phenomenon has been referred as relaxor-like behavior occurring in semiconductor ferroelectrics, $NaNbO_3$ [26] and $PbNb_2O_6$ [27], at cryogenic temperatures. Here, the apparent relative maximum of ε' at approximately 255 K also has been observed as function of the frequency of measurement. The dependence of a maximum value of permittivity with a frequency has been assigned to some degree of chemical and structural disorder. In accuracy with neutron diffraction analysis, and data analysis via Rietveld method, in $Sr_2KNb_5O_{15}$ a true relaxor-like behavior does not exist since the atoms occupy specific positions in the structure. Then, neither all TTB ferroelectric based on the niobium backbone seems be a relaxor. From data analysis, according to discussion of itens "Distortion Mode Analysis" and "Phase Transition, $Sr_2KNb_5O_{15}$" is mimetic relaxor. This find suggests the classification of niobium TTB. Here, the distinct site occupation by strontium and potassium ions is intrinsic feature since is a recurrent phenomenon. TTB polycrystal can be called of pentagonal IIA-IA class as $Sr_2KNb_5O_{15}$ and $NaSr_2Nb_5O_{15}$[3], which differ of compounds of class pentagonal IVA-IIA. This short formalism provides two strategies information about the niobium site that is relevant to the understanding of the thermal stability. After pentagonal, follows the chemical group of cation of highest electronegativity followed of chemical group of cation of lowest electronegativity. Therefore, the phenomenon observed at approximately 255 K as function of the frequency can be resulted of different domains in the structure, as observed in the electric response (Fig. 10). In addition, according to Fig. 14 the peak centered at close to 408 K exhibits a sharp absolute-maximum (ε' = 2375) in the ε'(ω) *versus* T curve and has been assigned to the ferroelectric-paraelectric transition [17] due the Curie's temperature. This peak does not depend on the measurement frequency, implying that the $Sr_2KNb_5O_{15}$ dielectrical behavior is close to the behavior of a classical ferroelectric. A single peak in the ε" (ω) versus T curve of small intensity, occurring as a broader peak at approximately 146 K, is attributed to the existence of

dielectric loss by conduction [28], since that ε”(ω) is assigned to conduction. The evolution of ε”(ω) versus T with the frequency shows that ε” (1 kHz) >> ε” (10 kHz) >> ε” (100 kHz) >> ε” (1 MHz). This behavior can be related to the interface contributions observed at low frequency (f < 1 kHz), as shown in Fig. 10.

During the cooling stage, when the cryogenic temperatures are reached, there is a tendency that the structure undergoes distortions, assuming a lowest symmetry [29]. As function of low thermal vibration of lattice, during this event occurs shrinkage of crystalline lattice from static disorder changing level, via oxygen sub-lattice displacement and sub-sequent re-positioning of niobium ion along c-axis, as well as re-dimensioning of the pentagonal cage ascribed to ion of group IIA and IA and tetragonal cage occupied exclusively by ions of IIA group, see previous discussion. Despite of small magnitude of atomic displacement as function of temperature, the electric charge displacement induced by electric field is several times more significant that allows magnitude and accuracy in the lattice-structure characterization. From this, free carriers or electrons that can be displaced by long range at low frequencies or frequencies reaching to zero are important, but charge moving by short range is reached in information about thermal lattice changing or distortion or phase transition being these phenomenon properly dimensioned by monitoring dielectric permittivity parameter. An analysis detailed of lattice phenomena of the $Sr_2KNb_5O_{15}$ induced by changing of the temperature has been realized taking into account the deconvolution of curve of the real part of complex dielectric permittivity response versus temperature, ε’(ω) *versus* T, points measured at 1 KHz during the heating cycle, as shown in Fig. 15. The deconvolution procedure has been successfully applied in analysis of structural phase transition phenomenon in niobates with perovskite structure and multiplicity of cell at unitary cell [16,30] in order to derive contributions of the distribution function of permittivities. Each distribution function represents an implicit thermally activated phenomenon describing a phase transition. A set of Gaussian functions has been used to adjust the experimental permittivity curve and a baseline was adopted [30]. In this procedure, the temperature of the anomaly is correlated to the major permittivity value and *vice-versa* being

considered the most frequent permittivity value that is the center of the distribution function. Here, prior to starting the adjusting procedure, the temperatures for fitting the center of distributions were previously identified constituted by four anomalies. The experimental curve is as far complex as more transition type of structural or of group space distortion. Seems natural that each phenomenon covers some interval of temperatures, since there is a gradual lattice distortion, and then is fact for a succession of event an entire range of temperatures is involved at transitions. The first anomaly is positioned at 146 K, the second one at 255 K, and the third positioned at 408 K (Curie's temperature). Another anomaly was identified from visual inspection of the curve, positioned at around 459 K. However, others anomalies beyond of interval of temperature modeled can be identified in regions of intersection (I) of the curve of deconvolution. The first intersection point at is positioned at 185K (I1) and a second one occurs at 340K (I2). Therefore, there are six temperatures associated direct or indirectly with anomalies.

From discussion above, via analysis of the permittivity curve, there is the non structural phase transition detected at 255 K, which is also identified in the curves of Fig. 5 and 6. Furthermore, this non structural phase transition of the $Sr_2KNb_5O_{15}$ derived here at 255 K has been previously identified in other tetragonal tungsten bronze TTB-type structure as $(Sr_{0.61}Ba_{0.39})_5Nb_{10}O_{30}$, $(K_{0.5}Na_{0.5})_{1.0}(Sr_{0.75}Ba_{0.25})_{4.5}Nb_{10}O_{30}$, $K_{5.80}Li_{3.82}Nb_{10.12}O_{30}$ and $K_{5.20}Li_{2.34}Nb_{10.88}O_{30}$ crystals [5]. The remanent polarization estimated and dielectric constant showed similar shapes and values along the [100] and [110] axis, not showing any evidence for the polarization tilting toward the [110] axis [5]. Similar find in TTB-type tetragonal structure has been reported involving a structural phase transition from tetragonal to monoclinic phase, resulting of the polarization tilting from the *c*-axis [001] towards the [110] direction of a tetragonal cell [4]. In addition, in according to literature the low temperature anomalies in TTB-type structure should be related to a freezout of some dielectric polarizability effects in the plane perpendicular to the polar *c*-axis rather than the existence of another structural phase transition [5]. In addition, exist also the possibility of the formation of short-range polar ordering resulting in ferroelectrically active nano-

domains referred to the polar nanoregions (PNRs) as reported in $Sr_{0.61}Ba_{0.39}Nb_2O_6$ (SBN) [31]. In SBN the formation of PNRs occurs as a result of A-site disorder by the size difference between Ba^{2+} and Sr^{2+} and also by the random distribution of vacancies sites [31]. The formation and random distribution of these vacancies is suggested to create random electric fields which favor the alignment of polarized clusters. Despite of a nanometric/nanostructured ceramic be more complex that a crystal, the transposition of concepts, theories and hypothesis developed for crystal should be carefully analyzed. A remarkable characteristic of TTB crystal mentioned above is its non stoichiometric character and non conventional occupation from which structural features can be modulated. Summarizing, as a matter of fact, both crystals and polycrystal of class pentagonal IIA-IA and pentagonal IIA-IIA exhibit a transition at 255 K, which can be of type structural or non structural. This transition is naturally structural for crystal when tilting of niobium octahedron toke place, as discussed previously. In this sense, the displacive character of transition seems non coupled to disorder-order of static nature. This event put a new light on the non structural phase transition to $Sr_2KNb_5O_{15}$ ceramic highlighted be non structural being sufficient the static order-disorder phenomenon, as discussed previously. In $Sr_2NaNb_5O_{15}$ ceramic the anomaly observed in the dielectric constant at low temperature can not be assigned to the relaxor-like behavior resulting of the loss of the ferroelectric character due to the breaking of the long distance correlation in the ferroelectric domain as a result of the presence of polar nanoregions PNRs, with a classical disordered profile. The development of PNRs has been associated to the disordered occupation of A1 and A2 sites [24]. By hypothesis PNRs can be formed in $Sr_2KNb_5O_{15}$ nanoceramic being assigned to the Nb-site distinct distortion. From previous analysis of the neutron diffraction data suggests that the dipolar response in these materials is predominantly linked to the Nb site occupation of type 1, Nb(1). From structural refinement, Nb^{5+} cations can be differentiated as Nb(1) and Nb(2) because they occupy two non-equivalent octahedral sites called B1 (*2b* sites) and B2 (*8d* sites) [3], as shown in Tables 3 and 4. One of the characteristics of TTB-type niobates is the intra-octahedral distortion of the Nb^{5+} cation. The off-center position of the Nb^{5+} cation and octahedral distortion have been

attributed to second-order Jahn-Teller (SOJT) effects as well as to the factors as bond networks, lattice stresses in the solid-state framework and punctual defects in the crystalline lattice [3]. In according to reported previously, in this work, the Nb-O average distances in both Nb(1)-O_6 and Nb(2)-O_6 octahedral show a significant relative off-centre displacement of Nb parallel to *c*-axis, leading to unequal Nb(1)-O(5) and Nb(2)-O(3) bond lengths, as shown in Fig. 4. Then, in a broad sense, due the stronger anisotropy, double occupation niobium site occupation, double occupation of pentagonal site by alkaline and alkaline earth, the first order phase transition discharged with crystalline symmetry being invariant with a serie of phase transitions type ferroelectric-ferroelectric based on the maintainment of space group but allowing its distortion and/or changing.

Fig. 16 shows the evolution of ε' at 1 kHz measured during a thermal cycle. The ε' parameter exhibits a clear and well-behavioured thermal-hysteresis at cryogenic temperatures domain, see the dashed area. The thermal hysteresis reach to 61 K at ε' equal to 1336. Typically, mixture of phases of same stoichiometry but distinct symmetry structure gives the above mentioned hysteretical effect[30]. In fact, the *si ne qua non* condition is the co-existence of phases of same symmetry but with a particular crystalline lattice distortion. This concept is relevant since transitions might be structural or not. If sufficient degree of distortion is generated a new symmetry can emerge, otherwise the phase transition occurs but the prototype symmetry is maintained while only specific distortions are permitted in accordance with niobium-off-center distortion. *A priori*, the further example of a complex sequence of phase transitions with absence of symmetry changing is given by $NaNbO_3$ [32]. In this case, the prototype phase is differenced along of the sequence adopting a simple superscript indexer as, orthorhombic', orthorhombic", orthorhombic"', etc [33]. Taking into account discussions of Fig. 14, 15 and discussion immediately above, a significant area of thermal hysteresis below 408 K strongly suggests that there are not a structural phase transition corroborated by the specific lattice parameter evolution and that non exhibits discontinuous or abrupt changing. Then, significant part of the phenomenon has only basis on the structural distortion. The systematization of TTB class can be structured as follows. As previously mentioned, the TTB-type

structures belong to the class pentagonal IIA-IA meaning pentagonal site is occupied by IIA group (alkaline earth metal) ions and IA group (alkaline metal), as well as tetragonal sites occupied only by IA group ions. The pentagonal sites called A2-sites contain a fraction of cations with remarkable preference by tetragonal sites called A1-sites as an example lead or strontium. Here, *a priori*, same stoichiometry and symmetry are maintained but distinct space groups were stabilized by set of distinct interfaces and stress/strain phenomenon acting under coordination polyhedra. In this way, co-existence of crystalline domains with a same prototype space group but with different distortion occurs during a cooling/heating process. The phenomenon and its origin are not universal for TTB niobate covering a specific class of niobates with tetragonal tungsten bronze structure. It is worth noting that classification given here provides the following information structural site as follows: relevance to lattice stability succeeded of the position that these cations occupy in the Periodic Table, as an example the type IIA-IA (element of IIA group: Sr followed of element of IA group: K and). In this sense seems that most general class is the class pentagonal IIA-IIA, as an example have the barium strontium or barium calcium TTB niobates. As above mentioned, the class pentagonal IVA-IIA is represented by lead strontium niobate of TTB structure. All niobate mentioned previously have in common the structural C site empty. There is another common characteristic between these TTB niobates that can be the key of the classification of them with relation to the structural thermal stability, which is a function of the position of chemical element in Periodic Table. From this view-point, seems that the electronegativity of ions that occupy pentagonal and tetragonal sites of TTB niobate determines a part of thermal structural stability of lattice. Highly electronegative ions (≥ 2.33) occupying the pentagonal sites and low electronegative ions at tetragonal sites give a lattice typically with symmetry lower than tetragonal at cryogenic temperatures and subsequent phase transition during heating; this case seems be of the class pentagonal IVA-IIA. Electronegativity values at low values level (~ 0.82) of ions occupying in a major way pentagonal site and intermediate values level (~ 0.95) of ions occupying a major way tetragonal sites give rise further crystallographic ambient that a priori is not favourable to the

changing of crystalline symmetry. These conditions satisfy the class pentagonal IIA-IA and IIA-IIA. If both pentagonal and tetragonal sites are occupied by ions of low electronegativity (≤ 0.82) giving the class pentagonal IA-IA. In fact, the participation of pentagonal and tetragonal sites occurs in an indirect way. In the practice, during shrinkage of lattice at cooling cycle, niobium-off-center tends to increment its shifting from center of oxygen octahedron (B sites). Since the niobium-off-center magnitude has a limit, the classical tetragonal stress phenomenon stay established being the extension along c-axis should be of dimension of niobium octahedral ≈ 4 Å. For sake of the retrieving of acceptable level of stress the [NbO6] octahedron should rotate, but not in a free way. Niobium sites form two types of niobium octahedron rings, see Fig. 17, being the distortion of each member of ring occurs in a cooperative process during continuous release of structural stress thermally induced. In fact, the ring is based on oxygen of the basal plane of each niobium octahedron. However, the magnitude of the cooperativity is modulated by second coordination sphere addressed to both pentagonal and tetragonal sites that interact with niobium octahedral via the corner sharing. Really, the tetragonal sites have as neighbourhoods only the octahedra of Nb(2), while pentagonal sites are neighbourhoods of octahedral of Nb(1) and Nb(2). Seems that at the moment the phenomenon has not a proper designing then from this point the phenomenon will be called of Pulsation of the Niobium Octahedra O-Ring or PNOOR effect. The PNOOR effect is determined by a distortion of niobium octahedral based on the octahedral compression and/or rotating. The existence of tilting phenomenon will have strong implications under stability of system crystalline, since as function of tilting should occur a displacement of niobium at new position of basal plane of octahedron perpendicular to the c-axis. This particular displacement would be accomplished of structural phase transition since a second stable position at niobium will be generated. From previous discussion, the tilting phenomenon does not occur here, see Symmetry-mode analysis in the section "*[NbO_6] Distortion Mode Analysis*" .

Taking in account the PNOOR effect, the compression process of a niobium octahedra is connected to pentagonal site occupied by an ion of intermediate/high electronegativity, as the Sr/Pb

ion. This feature can be understood as follows: the O-ring of niobium octahedra has five niobium octahedron and only one of these octahedron is of the type Nb(1), four of these niobium octahedral are of type Nb(2); the unique octahedron of the type Nb(1) exhibits a lowest level of distortion, while all four octahedra of the type Nb(2) exhibit a significant distortion level; the pentagonal site is called of A2, see Fig 17 discussion; the O-ring of five octahedra gives origin to a pentagonal site occupied by potassium and strontium cations; On the other hand, two Nb(2) octahedra accompanied of others two Nb(2) niobium octahedra belonging to another ring forming a square-ring containing four Nb(2) octahedra that give origin to the tetragonal site A1 being all octahedral exhibits very low or absent average rotation degree. Further investigations are necessary to determine if rotation leads to compression or the compression of $[NbO_6]$, site A2, leads to rotation of $[NbO_6]$, site A2. However, here, is evident that rotation of $[NbO_6]$ is facilitates by the level of the electronegativity of pentagonal cations from low to intermediate. Since, oxygens belong to (ab)-plane and some niobium octraedron, as well as alkaline and alkaline earth polyhedron sharing a corner, distortions of niobium octahedron take place with changing of the off-center position which is accommodate by changing of bond length of basal plane of octahedron. The Nb(2) that coordinates the pentagonal site occupied by alkaline cation (K) and alkaline earth cation (Sr) exhibits a minor niobium off-center magnitude explicating some kind of compromise between shifting of niobium along c-axis and octahedron rotating along c-axis.

Conclusion

Tetragonal-tetragonal distorted phase transitions were detected from neutron diffraction. The thermal lattice stability is assigned in a major way to cooperative interaction of niobium octahedra belong to the ring of five niobium octahedral and a minor way to the pentagonal cage, coordinated by five [NbO6], occupied in specific by potassium ions. The low electronegativity of K^+ allows intense distortion of chemical bonds shared with [NbO6] in an effect called PNOOR. This effect restrains the thermal shifting of Nb^{5+} along c-axis, such restriction actuates as an intrinsic guard mechanism counter-tilting of [NbO6], without a second position at niobium ions in (ab)-plane structural phase transition is impeded being favored the space group changing or distortion generated by re-accommodation of oxygen and niobium in a new [NbO6] configuration. In the cryogenic temperature domain of the permittivity curve, the large area of hysteresis below Curie's temperature of relative maximum was associated to the intrinsic structural distortion with major contributing of niobium that exhibits distinct degree of off-centering character. The distribution functions of the permittivity curve, derived by a set of Gaussian functions, can be related with implicit thermally activated phenomena. The electric response showed the presence of four equivalent circuits associated to the grain and different contributions of the grain boundary. Electrical phenomena of interface polarization are reviewed from microstructural, electrical and specific crystalline features. Frequency values of the interfaces can transmit signals of audio frequency. In this sense, the $Sr_2KNb_5O_{15}$ nanometric/nanostructured ceramic can be used as electroactive components in the ultra-low frequencies domain.

Acknowledgments

We thank FAPESP: contracts 2001/13421-7, 2002/05997-9, 2007/03510-9, 2012/23768-9 and 2013/17365-1; CNPq, CAPES and UNESP/PROPe, for their financial support, the Institut Laue Langevin for the use of neutron diffraction facilities and Prof. Dr. J. A. Eiras for electrical measurement at low temperatures.

References

[1] S. C. Abrahams , P. B. Jamieson and J. L. Bernstein, *J. Chem. Phys.*, 1971, **54**, 2355.

[2] S. Lanfredi, G. Palacio, F. S. Bellucci, C. V. Colin, M. A. L. Nobre, *J. Phys. D : Appl. Phys.*, 2012, **45**, 435302.

[3] S. Lanfredi, D. H. M. Gênova, I. A. O. Brito, A. R. F. Lima, M. A. L. Nobre, *J. Solid State Chem.*, 2011, **184**, 990.

[4] Y. Xu, Z. Li, W. Li, H. Wang and H. Chen, *Phys. Rev. B*, 1989, **40**, 11902.

[5] J. H. Ko, S. Kojima, S. G. Lushnikov , R. S. Katiyar, T. H. Kim and J. H. Ro, *J. Appl. Phys.,* 2002, **92**, 1536.

[6] H. Yan Guo, Ch. Lei and Z. G. Ye, *Appl. Phys. Lett.,* 2008, **92**, 172901.

[7] S. Lanfredi, I. A. O. Brito, C. Polini and M. A. L. Nobre, *J. Appl. Spectrosc.*, 2012, **79**, 254.

[8] F. S. Bellucci, E. R. Budemberg, M. A. L. Nobre, J. A. de Saja, R. F. Aroca, M. A. Rodríguez-Pérez and A. E. Job, *Sci. Adv. Mater.*, 2013, **5**, 637.

[9] S. Alkoyw and C. Duran, *J. Am. Ceram. Soc.*, 2008, **91**, 1597.

[10] J. Matos, P. S. Poon, S. Lanfredi and M. A. L. Nobre, *Fuel*, 2013, **107**, 503.

[11] G. A. Samara, E. L. Venturini and V. H. Schmidt, *Phys. Rev. B*, 2001, **63**, 184104.

[12] M. P. Pechini, U.S. Pat, No. 3.330.697, 1967.

[13] J. R. Carvajal, *An introduction to the Program FullProff 2000,* CEA/Saclay, France, 2008.

[14] G. K, Williamson and W. H. Hall, *Acta Met.*,1953, **1**, 22.

[15] K. S. Cole and R. H. Cole, *J. Chem. Phys.*,1941, **9**, 341.

[16] M. A. L. Nobre and S. Lanfredi, *J. Phys. Condens. Matter.*, 2000, **12**,7833.

[17] H. El A. Belghiti, A. Simon, P. Gravereau, A. Villesuzanne, M. Elaatmani and J. Ravez, *Sol. State Sci.*, 2002, **4**, 933.

[18] J. M. Perez-Mato, D. Orobengoa, M. I. Aroyo, *Acta Cryst. A*, 2010, **66**, 558.

[19] J. C. Tolédano, V. Janovec, V. Kopsky´, J. F. Scott and P. Boc˘ek, *International Tables for Crystallography*, Kluwer Academic Publishers, London, 2006, vol. D, Chapter 3.1.

[20] P. B. Moore, S. J. Louisnathan, *Zeitschrift fur Kristallographie*, 1969, **130**, 438.

[21] W. D. Kingery, H. K. Bowen and D. R. Uhlmann, *Introduction to Ceramics*, John Wiley & Sons, Inc., New York, 1977, p. 452.

[22] S. Lanfredi, M. A. L. Nobre, *Appl. Phys. Lett.*, 2002, **81**, 451.

[23] B. A. Boukamp, *Equivalent Circuit-EQUIVCRT Program-Users Manual*, University of Twente, 1989, **3**, 97.

[24] A. Torres-Pardo, R. Jiménez, J. M. González-Calbet and E. García-González, *Inorg. Chem.*, 2011, **50**, 12091.

[25] D. Viehland, S. G. Jang, L. E. Cross, M. Wutting, *J. Appl. Phys.*,1990, **68**, 2916.

[26] A. A. Bokov, Z. G. Ye, *J. Mater Sci.*, 2006, **41**, 31.

[27] J. de los S. Guerra, M. Vernet, D. Garcia, J. A. Eiras, F. Guerrero, *Appl. Phys. Lett.*, 2007, **91**, 062915.

[28] S. Lanfredi, M. H. Lente, J. A. Eiras, *Appl. Phys. Lett.*, 2002, **80**, 2731.

[29] C. Muller, J.L. Baudour, C. Bedoya, F. Bouree, J.L. Soubeyroux, M. Roubin, *Acta. Crystallogr B.*, 2000, **56**, 27.

[30] M. A. L. Nobre, S. Lanfredi, *J. Phys. Chem. Solids.*, 2001, **62**, 1999.

[31] W. Kleemann, J. Dec, V.V. Shvartsman, Z. Kutnjak, T. Braun, *Phys. Rev. Lett.,* 2006, **97**, 065702.

[32] R.J.C. Lima, P. T. C. Freire, J. M. Sasaki, A.P. Ayala, F. E. A. Melo, J. Mendes Filho, K. C. Serra, S. Lanfredi, M. A. Lente, J. A. Eiras, J. Raman Spectrosc., 2002, **33**, 669.

[33] H. D. Megaw, Ferroelectrics, 1974, **7**, 87.

Figure Captions

Figure 1: Thermal evolution of neutron diffraction pattern in the temperature range from 10 to 550 K.

Figure 2: The Rietveld refinement plot for $Sr_2KNb_5O_{15}$ with the experimental, calculated and difference neutron diffraction profile at 10 K (SG: P 4bm) and at 550K (SG: P 4/mbm).

Figure 3: $Sr_2KNb_5O_{15}$ structure refined at 550K. The position of K and Sr in the pentagonal site are split.

Figure 4: GM3- distortion mode of [NbO_6] represented around the two distinct niobium sites: Nb(1) in blue and Nb(2) in green. The directions of atomic displacement correspond to the direction of the arrows.

Figure 5: Thermal evolution of unit cell volume between 15 to 550 K. The lines going through the points are error bars.

Figure 6: Thermal evolution of lattice parameters a and c between 15 to 550 K. The red line is a guide for the eyes. The lines going through the points are error bars.

Figure 7: Crystal shape of fresnoite [20].

Figure 8: SEM image of the $Sr_2KNb_5O_{15}$ ceramic sintered at 1553 K for 2 h.

Figure 9: Expanded region of SEM image of the $Sr_2KNb_5O_{15}$ ceramic sintered at 1553 K for 2 h.

Figure 10: Experimental and theoretical curves of $Sr_2KNb_5O_{15}$ obtained at 600 K. Numbers 1, 2, 3 and 4 give the log10 (signal frequency) for the corresponding point.

Figure 11: Equivalent circuits obtained at 600 K.

Figure 12: Schematic diagram showing the development of deformation of the grain in the cleavage phenomenon.

Figure 13: Real and imaginary components of the impedance normalized by the geometric factor for the $Sr_2KNb_5O_{15}$ ceramic obtained at 600 K, with the adjustment curve generated from the Eq. (11).

Figure 14: Evolution of the real (ε') part and imaginary (ε") part of the complex dielectric permittivity of $Sr_2KNb_5O_{15}$ ceramic during the heating cycle, measured at different frequencies and temperatures.

Figure 15: Measured (circle points) and fitted (straight line) permittivity as a function of temperature during the heating cycle.

Figure 16: Permittivity as a function of temperature measured during the heating and cooling cycle at 1 kHz.

Figure 17: Representation of the tetragonal tungsten bronze (TTB)-type structure of $Sr_2KNb_5O_{15}$ refined at 300K , where *A1*, *A2*, and *C* represent the tetragonal, pentagonal and trigonal sites, respectively.

Tables Captions

Table 1: Structural data for the $Sr_2KNb_5O_{15}$ powder and the experimental conditions.

Table 2: Average crystallite size (D) and lattice strain (η) values of the $Sr_2KNb_5O_{15}$ nanostructured powder along (*00l*) plane as a function of temperature.

Table 3: (a) The atomic parameters, atomic displacement parameters and relative occupancies obtained by the refinement of $Sr_2KNb_5O_{15}$ at 10K; (b) Thermal factor of O3 and O5 refined with an anisotropic model; (c) Bonds distances for $Sr_2KNb_5O_{15}$ at 10 K.

Table 4: (a) The atomic parameters, atomic displacement parameters and relative occupancies obtained by the refinement of $Sr_2KNb_5O_{15}$ at 550 K; (b) Thermal factor of O3 and O5 refined with an anisotropic model; (c) Bonds distances for $Sr_2KNb_5O_{15}$ at 550 K.

Table 5: Summary of mode decomposition of the $Sr_2KNb_5O_{15}$ compound with the experimental P4bm ferroelectric structure, indicating the amplitude (Å) of the two intervening irreducible representation (IR) distortion components at 10K.

Table 6: Resistance, Capacitance, Relaxation Frequency and n values derived from adjustment of the impedance diagram at 600 K.

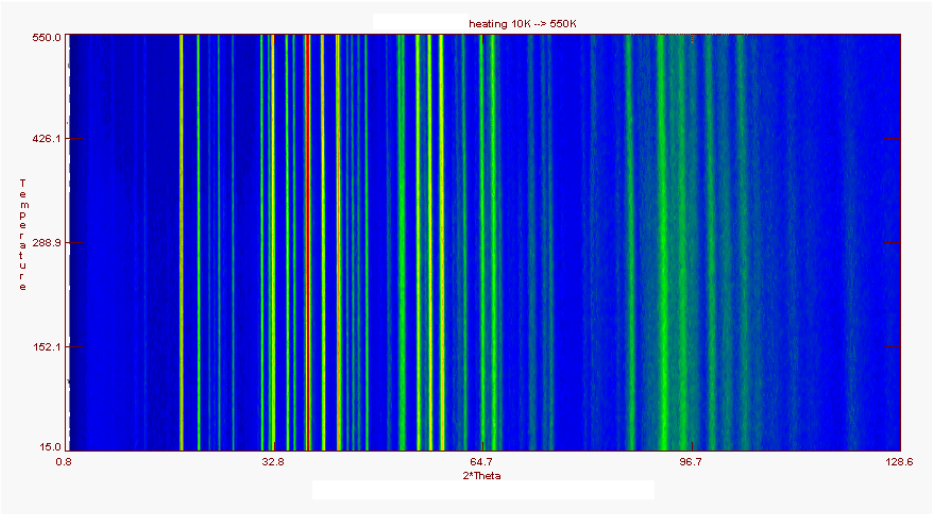

Figure 1

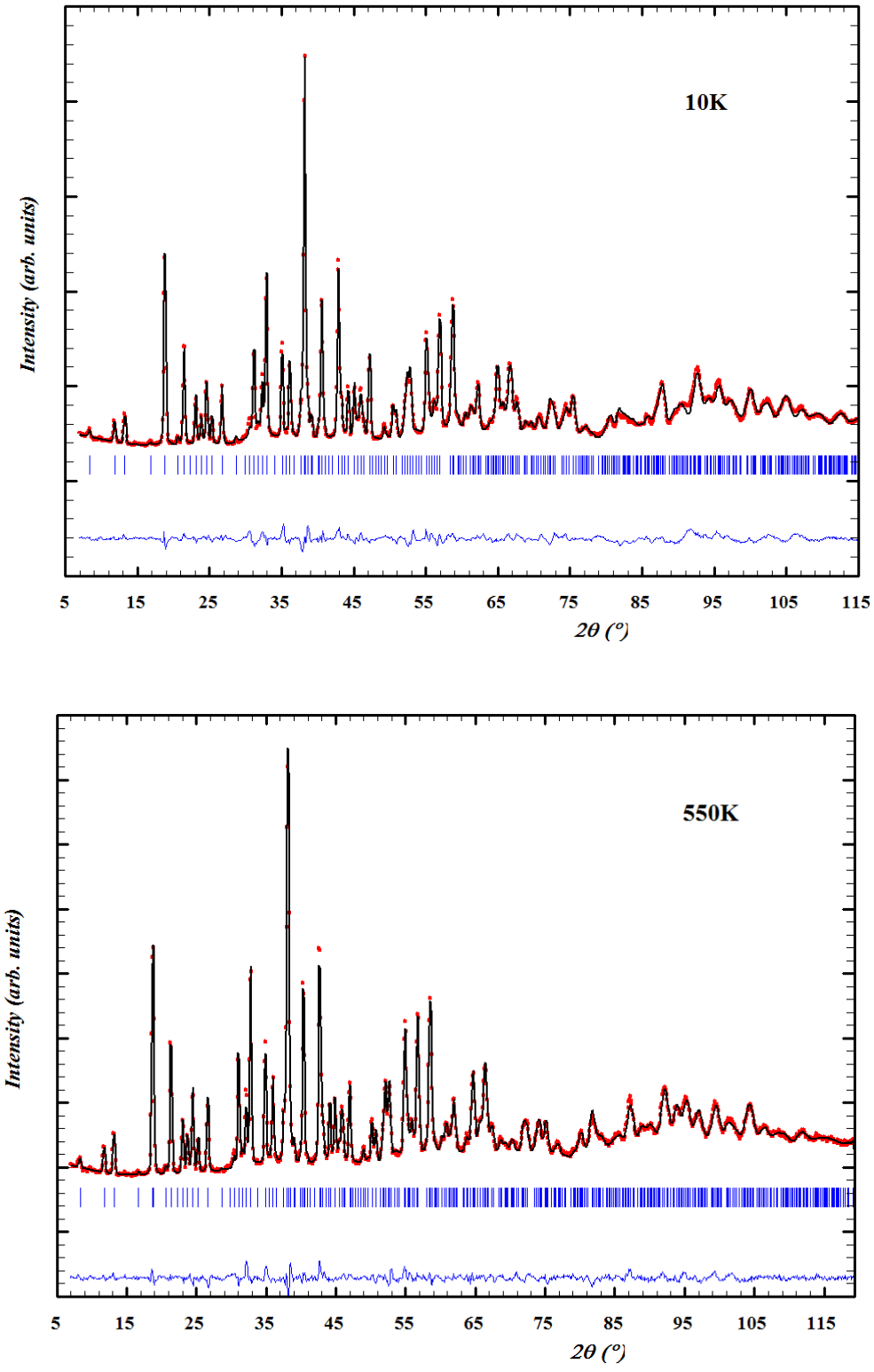

Figure 2

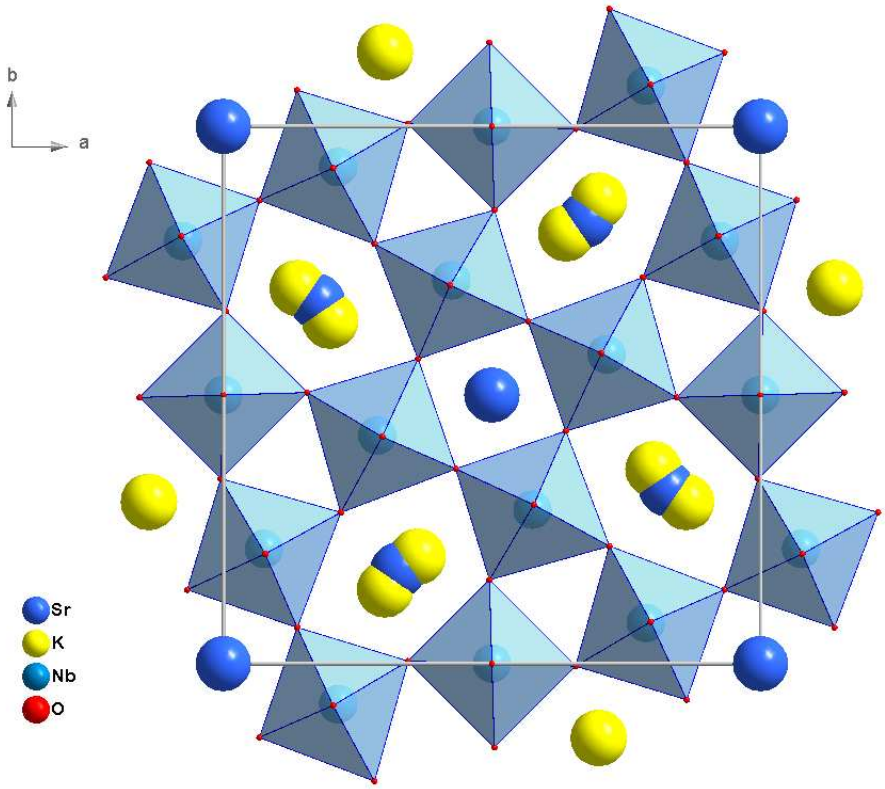

Figure 3

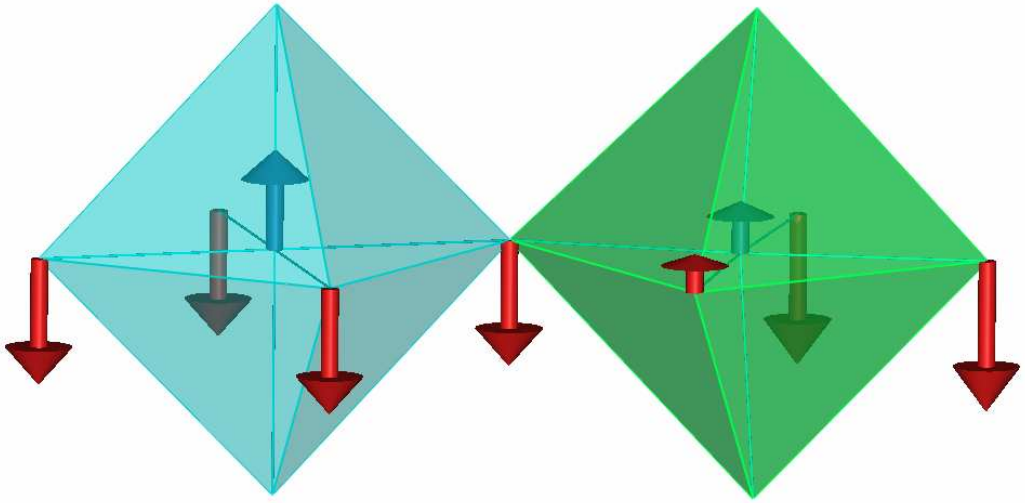

Figure 4

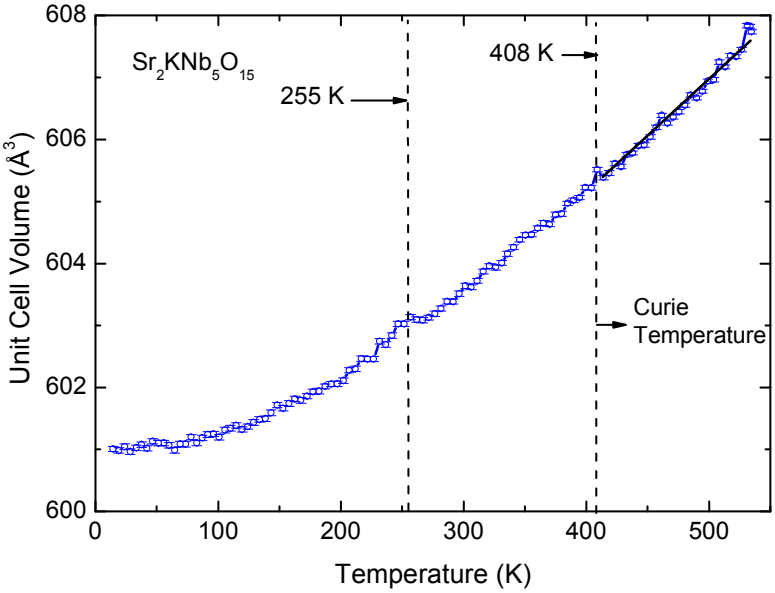

Figure 5

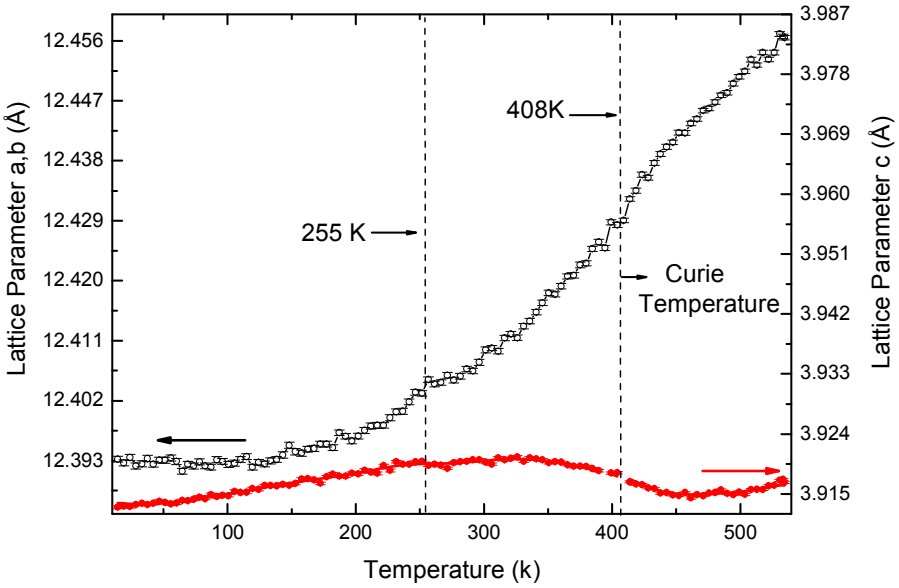

Figure 6

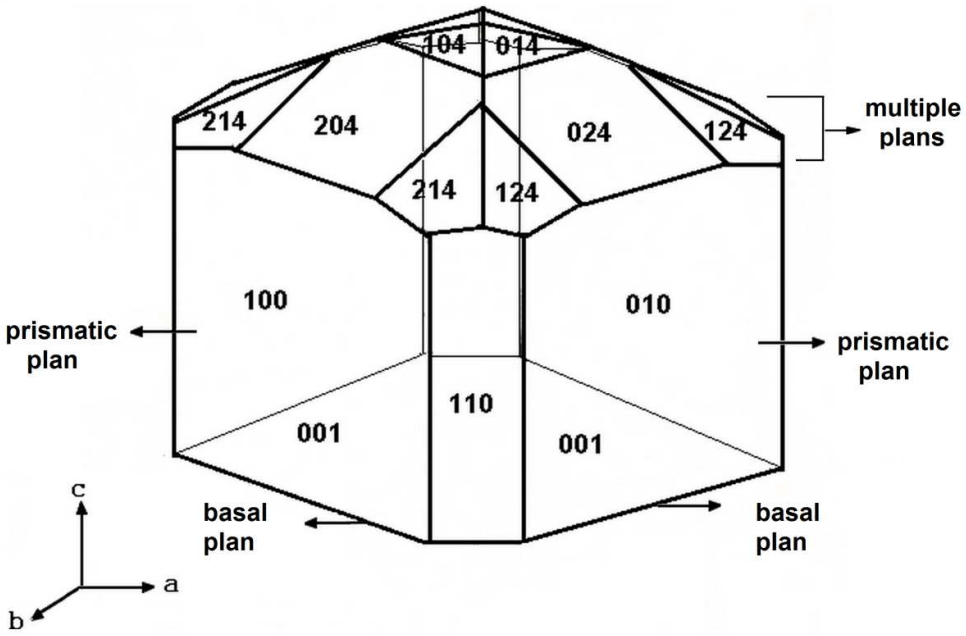

Figure 7

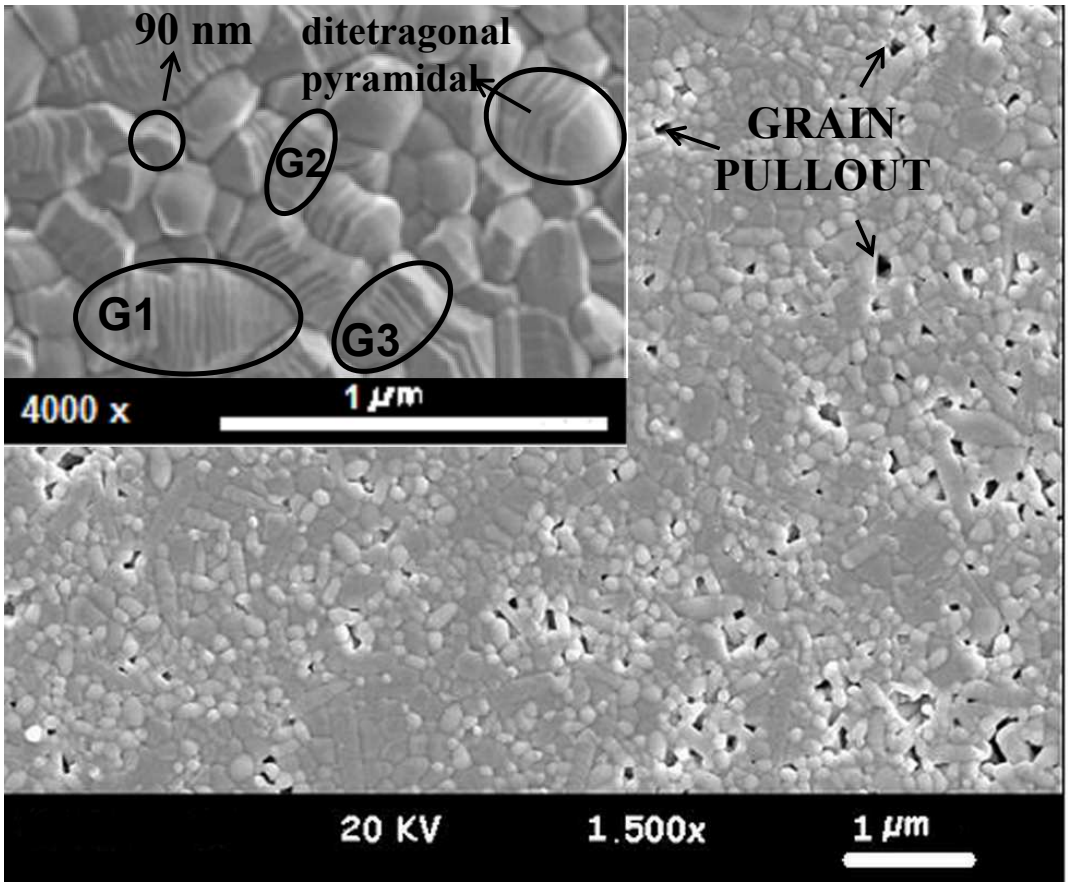

Figure 8

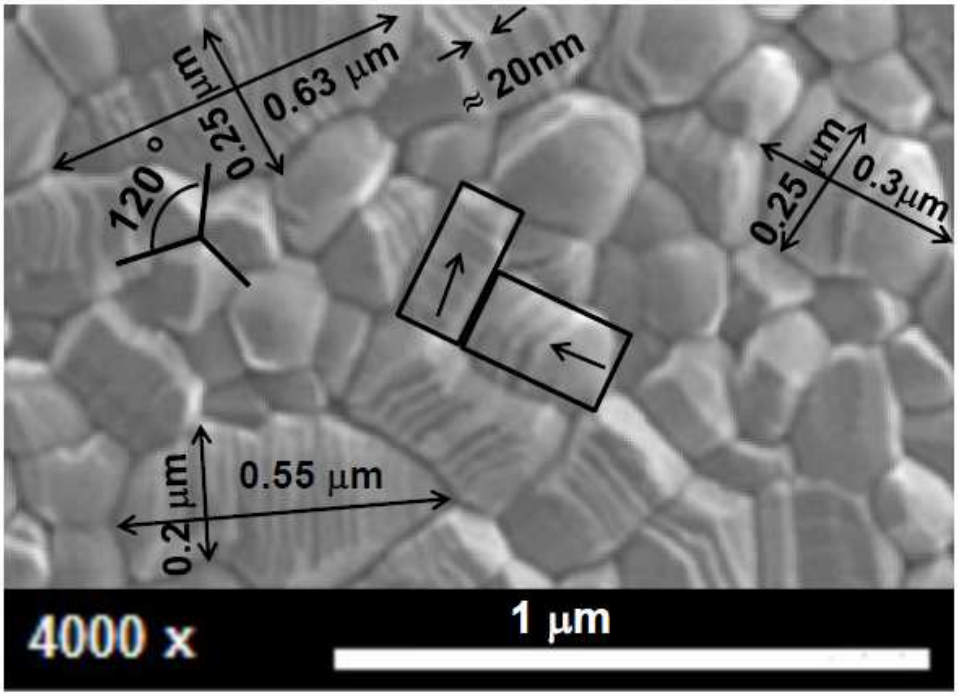

Figure 9

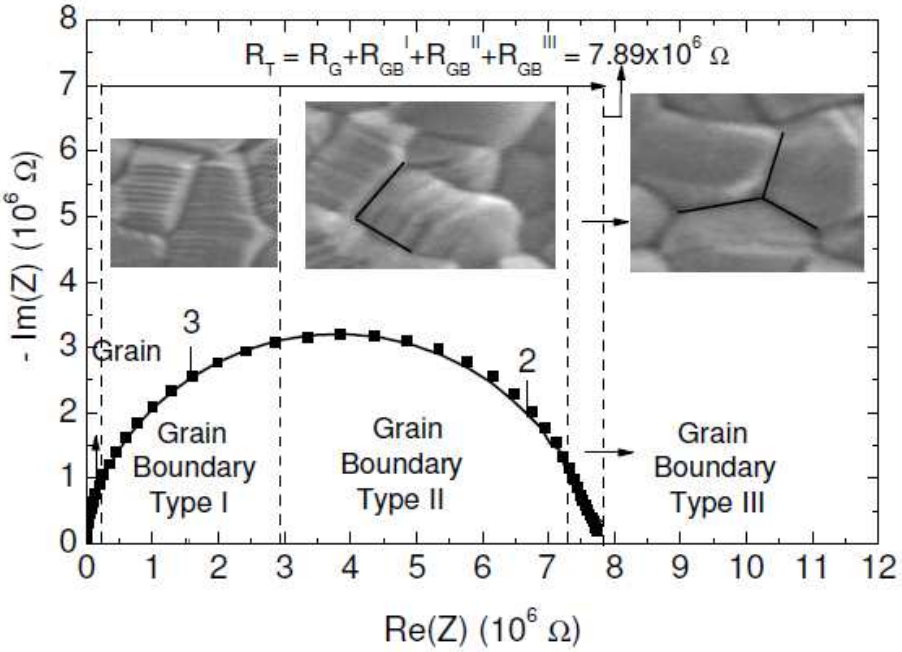

Figure 10

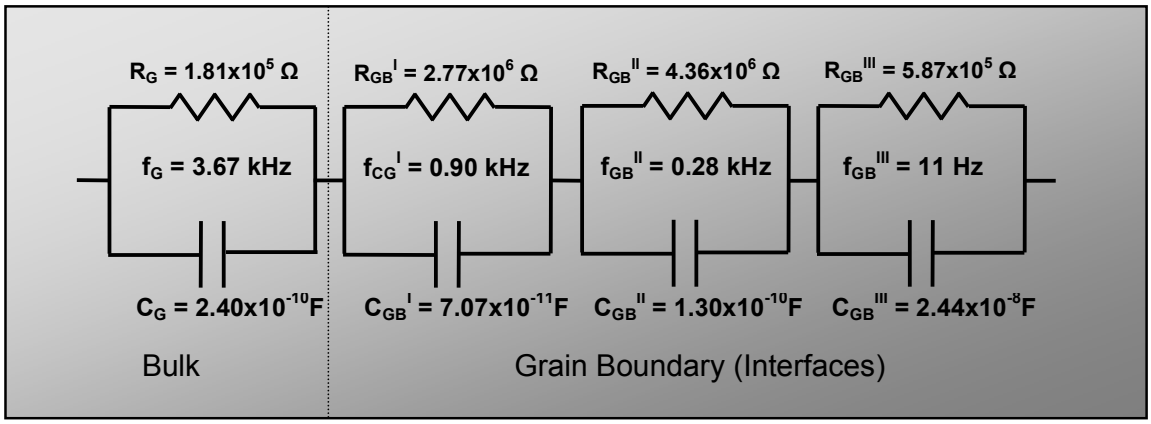

Figure 11

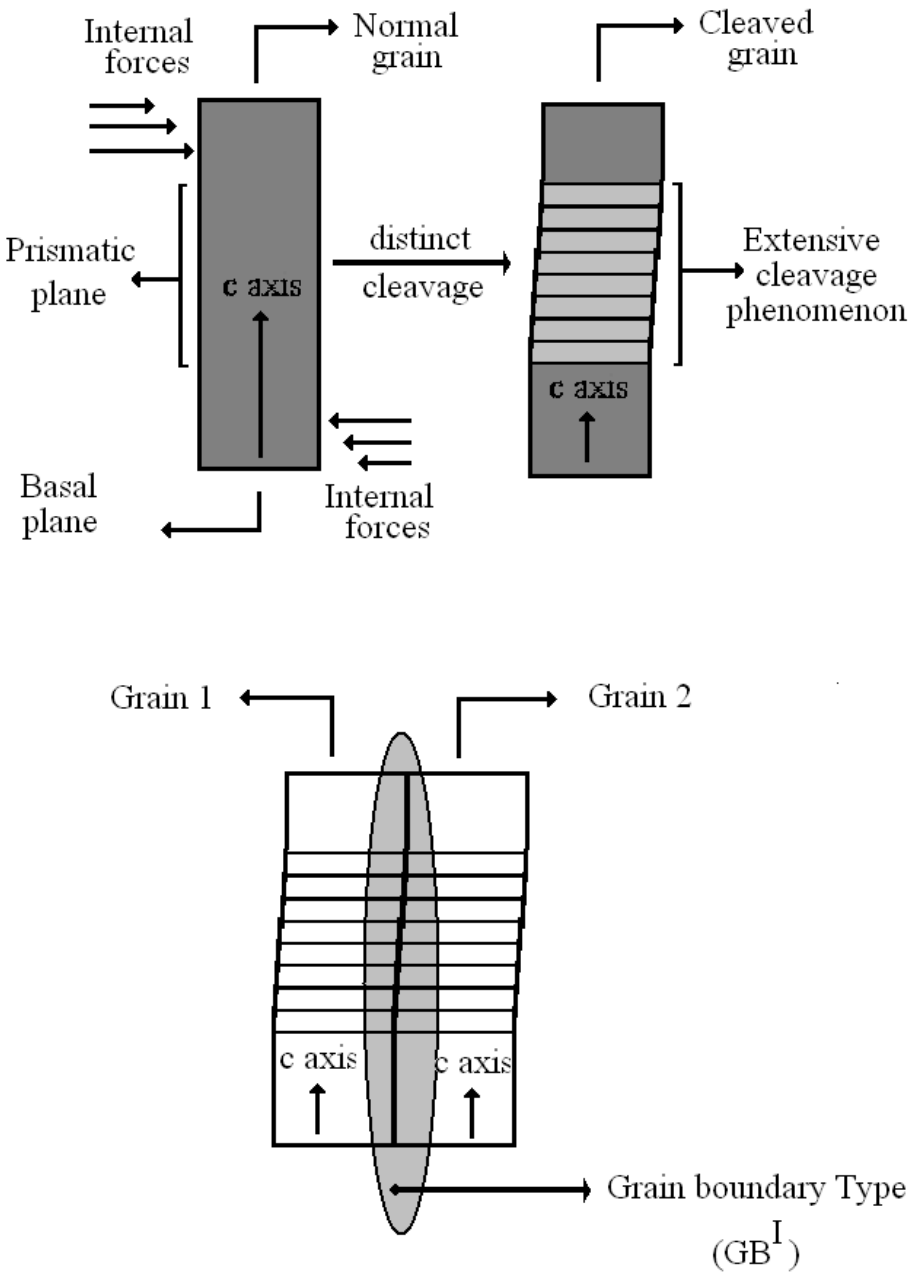

Figure 12

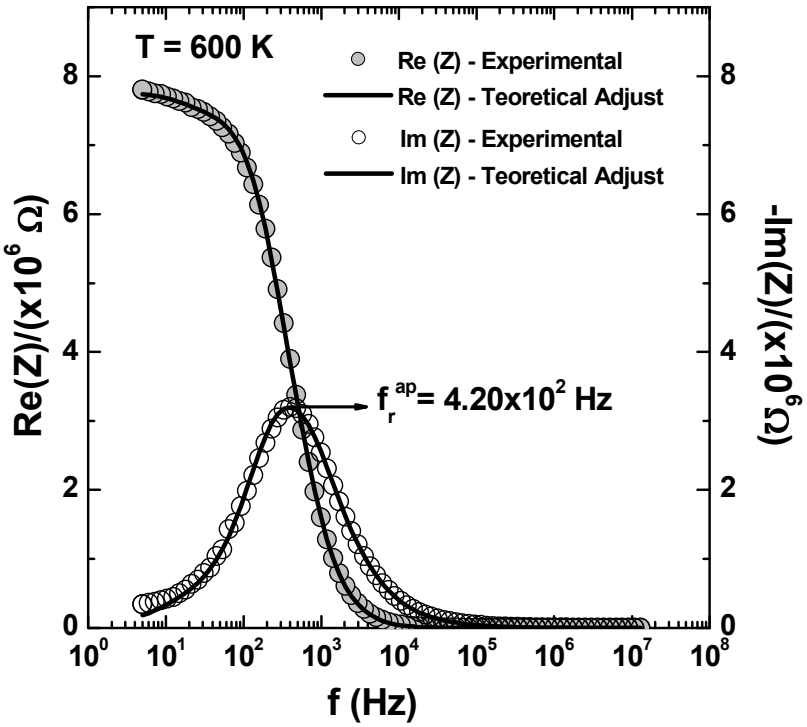

Figure 13

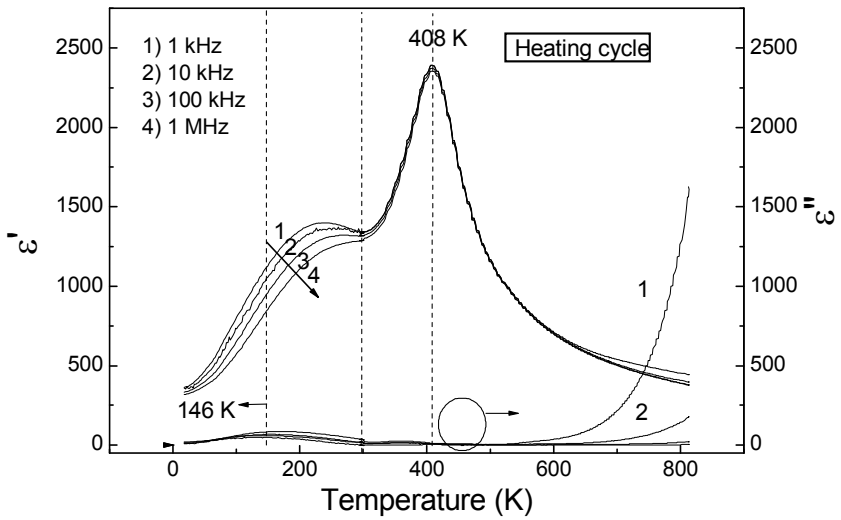

Figure 14

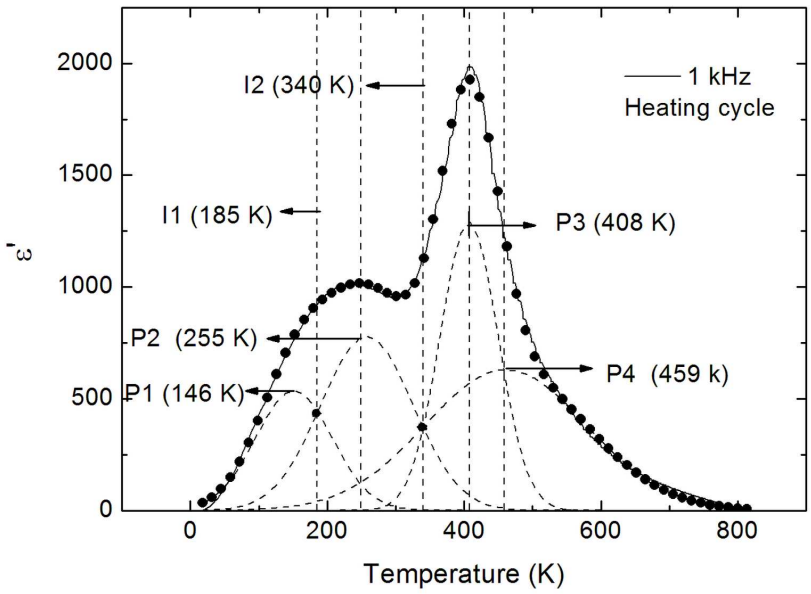

Figure 15

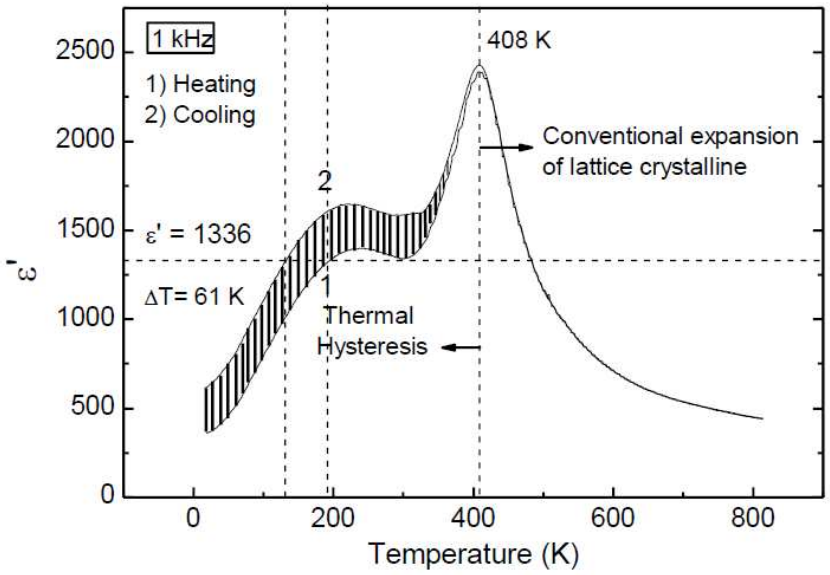

Figure 16

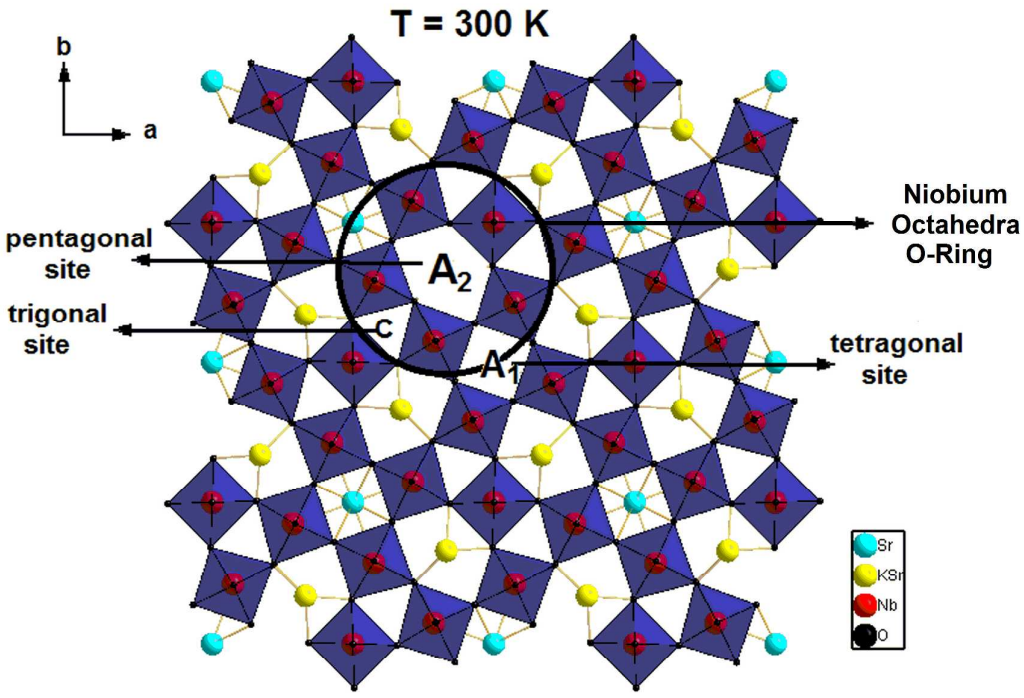

Figure 17

Crystallographic Data - $KSr_2Nb_5O_{15}$			
Temperature	10 K	300 K	550 K
Crystal system	Tetragonal	Tetragonal	Tetragonal
Space group	P4bm(No. 100)	P4bm(n°100)	P4/mbm(n°127)
a [Å]	12.3820(4)	12.3945 (3)	12.4450(3)
c [Å]	3.91023(15)	3.9151(9)	3.91329(11)
V [Å^3]	599.4927 (2)	601.4519(3)	606.0826(4)
Z	2	2	2
Data Collection			
Wavelength [CuK_α] [Å]	1.5418	1.5418	1.5418
Monochromator	Germanium	Germanium	Germanium
Measuring range (deg)	$0.8 \leq 2\theta \leq 128.0$	$0.8 \leq 2\theta \leq 128.0$	$0.8 \leq 2\theta \leq 128.0$
Rietveld Data			
Program	FULLPROF	FULLPROF	FULLPROF
$(H^2 = U\tan^2\theta + V\tan\theta + W)$			
U	1.3575 (4)	1.2625 (4)	1.3788 (4)
V	-0.7304 (2)	-0.7195 (2)	-0.8197 (2)
W	0.2087 (4)	0.2168 (4)	0.2284 (4)
R_{Bragg} (%)	5.78	4.28	3.99
cR_{wp} (%)	9.91	9.25	8.85

Table 1

T (K)	D (nm)	ε
10	20.0	5.275×10^{-4}
300	22.3	7.99×10^{-5}
550	20.2	4.15×10^{-4}

Table 2

Structure parameters of $KSr_2Nb_5O_{15}$ at 10K

Atoms	*Wyckoff Position*	x/a	y/b	z/c	$U_{(eq)}$ (Å^2)	*Temperature factor*	*Occ.*
Sr1	2a	0.00000	0.00000	0.00000	0.0060(15)	Uiso	1
K2	8d	0.1384(13)	0.6990(14)	-0.025(5)	0.00633	Uiso	0.25
Sr2	8d	0.17509	0.67346	-0.025(5)	0.00633	Uiso	0.25
Nb1	2b	0.00000	0.50000	0.473(5)	0.011(2)	Uiso	1
Nb2	8d	0.0752(3)	0.2138(3)	0.486(5)	0.0050(9)	Uiso	1
O1	8d	0.1378(4)	0.0658(4)	0.541(4)	0.0477(6)	Uiso	1
O2	8d	0.3457(4)	0.0046(3)	0.534(5)	0.0128(15)	Uiso	1
O3	8d	0.0785(7)	0.2028(4)	0.002(6)	0.047(4)	Uani	1
O4	4c	0.2816(4)	0.7816(4)	0.490(6)	0.017(2)	Uiso	1
O5	2b	0.00000	0.50000	0.000(10)	0.066(9)	Uani	1

Space group 'P 4 b m' (N°100): unit cell a=b=12.3820(4) (Å), c=3.91023(15) (Å), Rwp: 9.91, RBragg: 5.78

Table 3(a)

	U_{11}	U_{22}	U_{33}	U_{12}
O3	0.111(6)	0.019(4)	0.009(3)	-0.034(5)
O5	0.092(9)	0.092(9)	0.015(9)	-0.037(10)

Table 3(b)

Nb1 - O2 (x4)	1.926(6)
Nb1 - O5	1.85(4)
Nb1 - O5	2.06(4)
Nb2 - O1	2.001(7)
Nb2 - O1	1.995(7)
Nb2 - O2	1.918(6)
Nb2 - O3	1.90(3)
Nb2 - O3	2.02(3)
Nb2 - O4	1.962(6)

Bond distances (Å)

Table 3(c)

Structure parameters of $KSr_2Nb_5O_{15}$ at 550K

Atoms	*Wyckoff Position*	x/a	y/b	z/c	$U_{(eq)}$ (Å^2)	*Temperature factor*	*Occ.*
Sr1	2a	0.00000	0.00000	0.00000	0.0160(16)	Uiso	1
K2	8d	0.1383(19)	0.6991(18)	0.00000	0.01900	Uiso	0.25
Sr2	8d	0.17509	0.67346	0.00000	0.01900	Uiso	0.25
Nb1	2b	0.00000	0.50000	0.50000	0.0245(17)	Uiso	1
Nb2	8d	0.0756(3)	0.2135(3)	0.50000	0.0100(7)	Uiso	1
O1	8d	0.1374(3)	0.0672(4)	0.50000	0.0194(10)	Uiso	1
O2	8d	0.3440(4)	0.0046(3)	0.50000	0.0248(13)	Uiso	1
O3	8d	0.0779(5)	0.2043(4)	0.00000	0.037(3)	Uani	1
O4	4c	0.2813(3)	0.7813(3)	0.50000	0.0228(18)	Uiso	1
O5	2b	0.00000	0.50000	0.00000	0.048(6)	Uani	1

Space group 'P 4/m b m' (N°127): unit cell a=b= 12.4450(3) (Å), c= 3.91329(11) (Å), Rwp: 8.85, RBragg: 3.99

Table 4(a)

	U_{11}	U_{22}	U_{33}	U_{12}
O3	0.064(4)	0.037(3)	0.011(2)	-0.033(4)
O5	0.066(6)	0.066(6)	0.013(6)	-0.022(7)

Table 4(b)

Nb1 - O2 (x4)	1.942(5)
Nb1 - O5 (x2)	1.95665(6)
Nb2 - O1	1.976(6)
Nb2 - O1	2.014(6)
Nb2 - O2	1.906(6)
Nb2 - O3 (x2)	1.9602(4)
Nb2 - O4	1.971(5)

Table 4(c)

K-vector	IR	Direction	Isotropy Subgroup	Dimension	Amplitude (Å)
(0,0,0)	GM1+	(a)	P4/mbm (127)	13	0.0000
(0,0,0)	GM3-	(a)	P4bm (100)	10	0.7479

Table 5

	Resistance (Ohm)	C (F)	f_r (Hz)	n
Grain	1.81×10^{5}	2.40×10^{-10}	3.67×10^{3}	0.9848
Grain Boundary I	2.77×10^{6}	7.07×10^{-11}	9.0×10^{2}	0.9913
Grain Boundary II	4.36×10^{6}	1.30×10^{-10}	2.8×10^{2}	0.9908
Grain Boundary III	5.87×10^{5}	2.44×10^{-8}	0.11×10^{2}	0.8869

Table 6

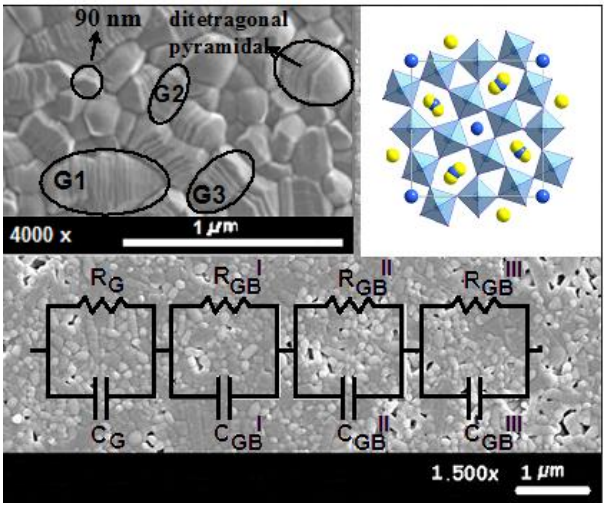

SEM image of the $KSr_2Nb_5O_{15}$ nanoceramic based on grains G1, G2 and G3 (90 to 500 nm) with the plot of the unit cell of the $KSr_2Nb_5O_{15}$ and set of the Equivalent circuits representing the several interfaces of the nanostructured ceramic.